



## 저작자표시-변경금지 2.0 대한민국

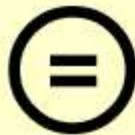
이용자는 아래의 조건을 따르는 경우에 한하여 자유롭게

- 이 저작물을 복제, 배포, 전송, 전시, 공연 및 방송할 수 있습니다.
- 이 저작물을 영리 목적으로 이용할 수 있습니다.

다음과 같은 조건을 따라야 합니다:



**저작자표시.** 귀하는 원저작자를 표시하여야 합니다.



**변경금지.** 귀하는 이 저작물을 개작, 변형 또는 가공할 수 없습니다.

- 귀하는, 이 저작물의 재이용이나 배포의 경우, 이 저작물에 적용된 이용허락조건을 명확하게 나타내어야 합니다.
- 저작권자로부터 별도의 허가를 받으면 이러한 조건들은 적용되지 않습니다.

**저작권법에 따른 이용자의 권리는 위의 내용에 의하여 영향을 받지 않습니다.**

이것은 [이용허락규약\(Legal Code\)](#)을 이해하기 쉽게 요약한 것입니다.

[Disclaimer](#)

2008年度

碩士學位論文

# Hull Form Development by Inverse Design method of Test result

실험 자료의 역계산법을 이용한 선형개발

朝鮮大學校 大學院

船 舶 海 洋 工 學 科

趙 景 勳

# Hull Form Development by Inverse Design method of Test result

실험 자료의 역계산법을 이용한 선형개발

2008년 2월 25일

朝鮮大學校 大學院

船 舶 海 洋 工 學 科

趙 景 勳

# Hull Form Development by Inverse Design method of Test result

실험 자료의 역계산법을 이용한 선형개발

指導教授 李 貴 珠

이 論文을 工學碩士學位 申請 論文으로 提出함.

2007년 10월

朝鮮大學校 大學院

船 舶 海 洋 工 學 科

趙 景 勳

趙 景 勳의 碩士學位論文을 認准함

委員長 朝鮮大學校 教授 朴 濟 雄 印

委 員 朝鮮大學校 教授 李 貴 珠 印

委 員 朝鮮大學校 教授 Igor Shugan

2007년 11월

朝鮮大學校 大學院

# TABLE OF CONTENTS

List of Table and Figures

Abstract

I. INTRODUCTION	.....	1
II. HULL GENERATION AND FOURIER NUBS METHOD	.....	3
A. Coordinate system	.....	3
B. Fourier expansion	.....	4
C. Hull generation	.....	5
D. Inverse transformation of the coordinate system	.....	8
E. Set of the surface net of control points for surface NUBS interpolations	.....	8
III. SHIPFLOW ANALYSIS	.....	9
IV. THE INVERSE DESIGN PROBLEM	.....	14
V. Examples	.....	17
VI. Conclusion	.....	25
Reference	.....	26

Appendixes

## TABLE OF TABLE AND FIGURES

Table 1

Fig. 1	Coordinate system to express the girth line	.....	3
Fig. 2	Transformed coordinate system for the girth line	.....	4
Fig. 3	Accuracy of curve fitting for various numbers of Fourier terms using NUBS functions.	.....	5
Fig. 4	Schematic figure for the location of control points on the Fourier NUBS curve	.....	7
Fig. 5	XMESH	.....	12
Fig. 6	Grid surrounding the aft half	.....	13
Fig. 7	Body plan of Series 60	.....	17
Fig. 8	Cp value of series 60 original. stem view	.....	18
Fig. 9	Cp value of series 60 original. Stern view	.....	18
Fig. 10	Cp value of series 60 original. Side view	.....	19
Fig. 11	Cp value of series 60 original. Bottom view	.....	19
Fig. 12	Comparison of girth lines with original lines	.....	20
Fig. 13	Front view of KCS	.....	21
Fig. 14	Bottom (Above) and side (Below) view of KCS	.....	21
Table 1	The principle particulars of KCS	.....	22
Fig. 15	Cp values of KCS	.....	22
Fig. 16	Comparison of body plans for Original(KCS) and Calculated (New KCS) hull form	.....	23
Fig. 17	Comparison of Cw for Original(KCS) and Calculated (New KCS) hull form	.....	23
Fig. 18	Comparison of Cv for Original(KCS) and Calculated (New KCS) hull form	.....	24

## ABSTRACT

### 실험자료의 역계산법을 이용한 선형개발

Cho, kyeong hoon

Advisor : Prof. Lee, Kwi-Joo, Ph. D.

Department of Naval Architecture

& Ocean Engineering

Graduate School of Chosun University

본 논문에는 주어져있는 선체주위 압력분포로부터 선박의 선형을 최적화하기 위한 역계산법을 이용하는 기술을 나타냈다. 모선 (Mother ship) 주위 압력분포를 변형하여 새로운 압력분포를 얻을 수 있다.

역계산법은 Levenberg-Marquardt Method (LMM)와 직접문제를 활용하여 개발되었다. 적은 수의 조정점(Control Points)으로 선형의 형상을 정의하기 위하여 Fourier Nonuniform B-spline(Fourier NUBS) 방법을 이용하여 선체표면을 정의하였다.

본 연구의 대상선형으로 Series 60선형과 KCS(KRISO 3600TEU CONTAINER SHIP)선형을 적용, 평가하였다. 결과적으로 요구하는 선형의 정밀도는 Fourier Nonuniform B-spline(Fourier NUBS)를 이용한 선체 표면 조정점의 수와 관련이 있으며, 충분한 조정점이 사용되었을 때, 만족할만한 최종 선형을 얻을 수 있다.



# 1. INTRODUCTION

The hydrodynamic performance of a vessel is strongly dependent on the shape of the vessel's hull. It is thus important that the form of the hull be carefully designed to achieve as optimal a performance as the constraints (i.e. the pressure distribution for the present study) will permit. This should be done at an early stage in the total vessel design schedule since any subsequent changes to the hull form may incur large costs resulting from other associated design modifications, for instance, the need to redesign bulkhead.

Traditionally, naval architects have based new hull designs on hulls already in service and known to perform well (i.e. parent ship), with any changes to the design being investigated using expensive model towing tank tests. In recent years advances in computational fluid dynamics have made possible the analysis of new, possible novel, hull forms at a fraction of the cost of model tests, with good estimates of the hydrodynamic forces acting on the vessel being obtained (Van Oortmerssen 1990).

The use of computational techniques, however, requires a numerical description of the hull shape. Various methods of defining the complex free-form shape of hulls for use in design optimization methods can be found in the literature ( Lin et al 1963, Wyatt & Chang 1990, Larsson & Kim 1992, Lowe et al 1994). However two user friendly methods of surface representation commonly used in the field of computer-aided design are Bezier and B-spline surface patches (Rogers & Adams 1990). Due to their simplicity, B-spline surface technique is used in this study.

Typically, the surface to be represented is broken into amesh of mainly rectangular curvilinear regions, for example, the areas formed by the section lines and waterlines of a vessel. A surface patch is then defined over each region, its shape being determined by a set of control points. These points form a polyhedrons which the surface approximates. The shape parameters in

this formulation are thus the coordinates of each control point, i.e. these limited number of control points become the parameters in controlling the hull surface geometry. In the present study the task is to redesign the bow of the ship based on previous hull shape and new desired pressure distribution. Therefore only the bow surface of hull is represented by B-spline surface.

With this in mind, the technique of inverse design problem should be used to design the new hull form in accordance with the desired pressure distribution for the bow of ship. This desired pressure distribution can be obtained by modifying the existing pressure distribution of the parent ship whenever one found that there exists a drastic change in pressure on the hull surface, since any drastic change in pressure represents flow separation or large drag force.

The direct problem involves the determination of the hull surface pressure distribution when the hull form is given. On the other hand the inverse design problem is concerned with the determination of the modified hull form from the given desired pressure distribution.

The present work addresses the development of an efficient method for parameter estimation, i.e. the Levenberg-Marquardt algorithm, in estimating the new hull form that satisfies the desired pressure distribution. The Levenberg-Marquardt method has proved to be a powerful algorithm in inverse calculations (Huang & Huang 1994, Huang & Ozisik 1991, Huang & Wang 1996), especially in parameters estimation.

The method of hull surface generation and B-spline surface fitting is described in Section 2. In Section 3 the method used to calculate the hull surface pressure distribution by SHIPFLOW, The inverse design problem involving the definition of cost function and Levenberg-Marquardt algorithm is addressed in Section 4. Finally a computational procedure is summarized in Section 5.

## II. HULL GENERATION AND FOURIER NUBS METHOD

### A. Coordinate system

The coordinate system which explains the present method [1] is shown in Fig 1.

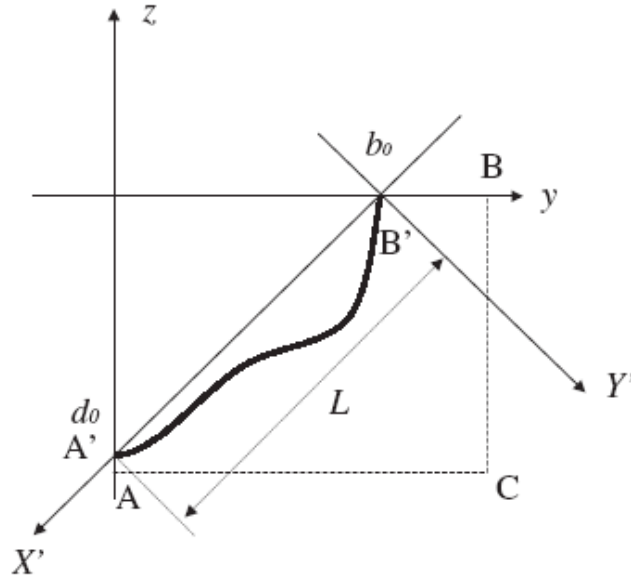


Fig 1. Coordinate system to express the girth line

The origin  $B'$  is set on the girth line on the  $y$ -axis. Then the  $X'$ -axis is chosen such that it goes from the origin toward the point of the girth line on the ship's center plane,  $A'$ . The  $Y'$ -axis is normal to the  $X'$ -Axis. Furthermore, the  $X', Y'$  coordinate system is normalized by  $L$ , the length of  $A'B'$ , and the newly derived coordinate system is written in the  $X, Y$  system, as shown in Fig 2.

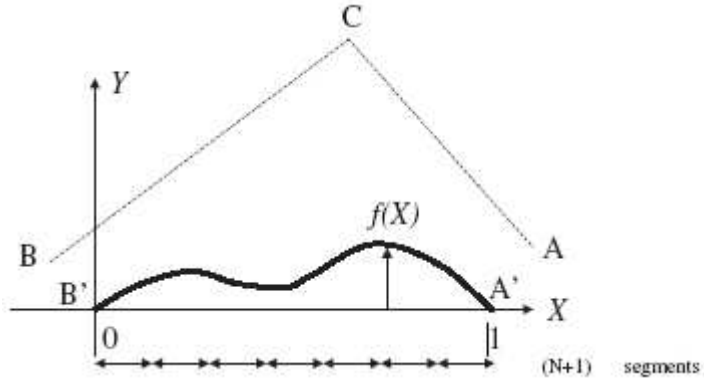


Fig 2. Transformed coordinate system for the girth line

## B. Fourier expansion

The basic idea of this method is that the control points of the NUBS function for expressing girth lines should be evaluated by the Fourier series. In order to set the control points for determining girth lines, we need suitable initial values of the coefficients of the Fourier series. In order to give suitable Fourier coefficients for the girth lines, we expand the basic ship's girth lines, say  $Y=f_{orig}(X)$ , into a Fourier series as follows:

$$f_{approx}(X) = \sum_{n=1}^N A(n) \sin(n\pi X) \quad (1)$$

$$A(n) = 2 \int_0^1 f_{orig}(X) \sin(n\pi X) dX$$

Note that  $f_{orig}(X)$  is the girth line of the basic ship in the transformed coordinates  $X, Y$ ,  $f_{approx}(X)$  represents the approximate girth line, which may contain some wiggles, and  $N$  is the number of terms of the Fourier series expansion.

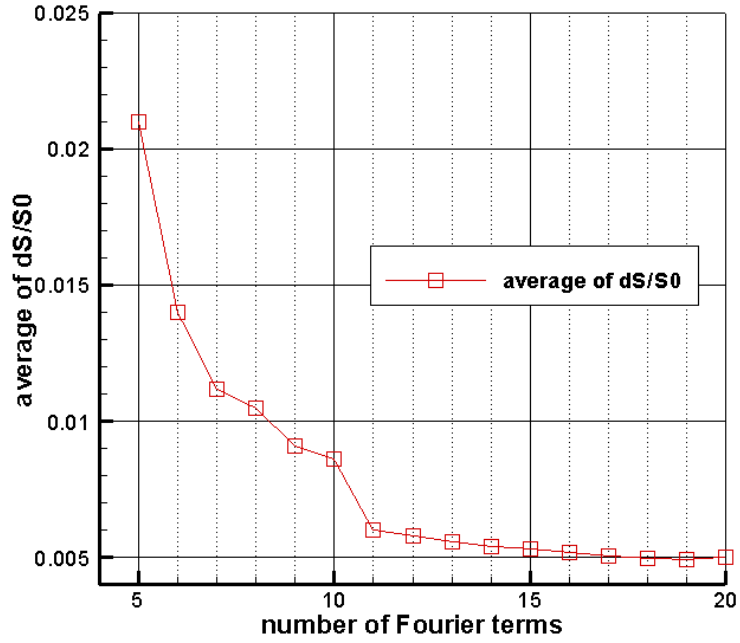


Fig 3. Accuracy of curve fitting for various numbers of Fourier terms using NUBS functions.

In order to investigate suitable value for  $N$ , define the area error due to the discrepancy of the girth lines as

$$\delta S/S_0 = \left( \int_{-d_0}^{decktop} |F_{approx}(x,z) - F_{orig}(x,z)| dz \right) / \int_{-d_0}^{decktop} |F_{orig}(x,z)| dz \quad (2)$$

where  $F_{approx}(x,z), F_{orig}(x,z)$  are the breadths of the calculated and original girth lines at  $(x,z)$ , respectively.

### C. Hull generation

The definition of a NUBS function [1] is

$$P(t) = \sum_{i=0}^{n-1} N_{i,m}(t) q_i \quad (3)$$

$$N_{i,m}(t) = \frac{t - t_i}{t_{i+m-1} - t_i} N_{i,m-1}(t) + \frac{t_{i+m} - t}{t_{i+m} - t_{i+1}} N_{i+1,m-1}(t), \quad (4)$$

$$N_{i,1}(t) = \begin{cases} 1 & (t_i \leq t < t_{i+1}) \\ 0 & (t < t_i, \quad t_{i+1} \leq t) \end{cases}$$

where  $q_i$  is the coordinates of the set of control points,  $m$  is the order of the NUBS function, which is set to 4 in this work;  $t_i$  is the set of knot vectors, and  $P(t)$  is the interpolated function. In this method, the X coordinates of the control points are determined as described below

1. Divide the  $0 \leq X \leq 1$  domain in to  $N+1$  equilength segments. Since the highest order of a Fourier series expansion is  $N$ , the number of segments should suit set  $N$  and not set  $N+1$ . However, numerical trials have shown that  $N+1$  divisions gives a much better results. Then the control points are located on both ends of each segment.

2. Near  $X=0$  and  $X=1$ , Fourier series expansions may not follow an original curve with a very large or small gradient, and in order to protect against this drawback, more control points are put around these regions. In this study, the  $ma$  and  $me$  segments adjacent to  $X=0$  and  $X=1$  are set and within in these segments, the number of control points are set at  $nc(ma)$  and  $nc(me)$ , receptively (Fig 4.).

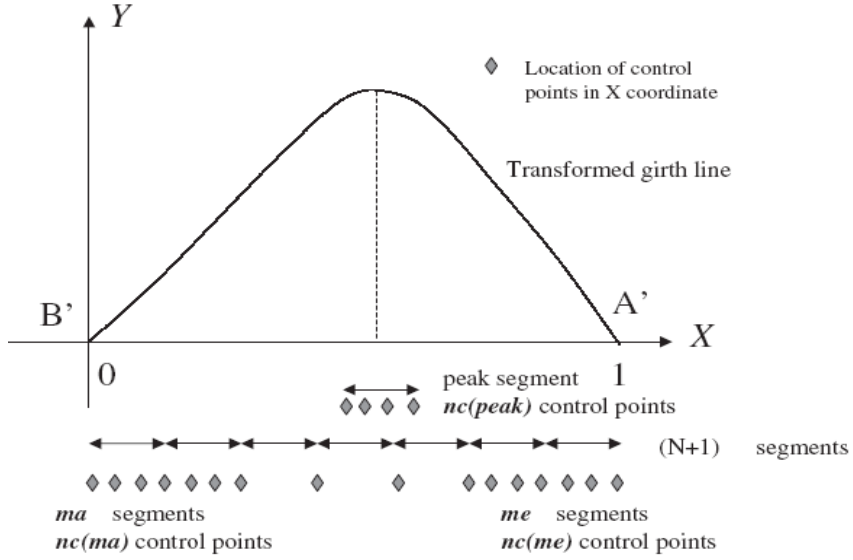


Fig 4. Schematic figure for the location of control points on the Fourier NUBS curve

3. The region around a peak point with a large curvature is also difficult to express without enough control points. In this work, only the region containing the highest peak point is used to set an additional  $nc(peak)$  control points. Here, the segment whose center coincides with the peak point is found, and then as additional  $nc(peak)$  control points are set in that segment. It may be necessary to use 4 or 5 points to reflect a sharp corner (Fig.4). In this study, the parameters  $ma$  and  $me$  are set to 2 for  $N \leq 10$ , and 3 for  $N \leq 11$ . In both cases,  $nc(ma)$  and  $nc(me)$  are 5 and  $nc(peak)$  is set to 4.

4. After determining all the X coordinates of the control points, the Y coordinates of the control points can be computed by the first part of Eq.1. In the computation of Y, if a control point exceeds limiting lines AC or BC, the control point is reset on the line. This process ensures that the computed girth line does not pass over the limitation line owing to the

convex hull properties of B-spline interpolation. After all the procedures are complete, the control points are established and then we can calculate the girth lines with the NUBS functions is Eqs.2 and 3. In this study, a uniformly distributed knot vector was used. Then the NUBS function becomes a simple B-spline function. Alternatively, we can use the equation

$$\begin{aligned} t_0 = \dots = t_{m-1} = 0, & \quad t_m = \dots = t_{n+m+1} = 1, \\ t_{j+m-1} = \frac{1}{m-1} \sum_{i=j}^{j+m-2} S_i, & \quad (j=1, \dots, n-m) \end{aligned} \quad (5)$$

where  $n$  is the number of control points,  $m$  is the order of NUBS, and  $S_j$  is often taken as the distance along the set of the given points.

#### D. Inverse transformation of the coordinate system

After setting all the control points, a new girth line is calculated by the NUBS function. Then the curve in  $X, Y$  space is inversely transformed so that the Fourier NUBS girth line can be obtained in  $(Y, Z)$  space. In this method, note that one girth line can be expressed with  $N+2$  design parameters, i.e., breadth at the deck top  $b_0$ , and depth  $d_0$ , and  $N$  coefficients of the Fourier sine series.

#### E. Set of the surface net of control points for surface NUBS interpolations

Consider the net of points on the surface  $P_{i,j}$  and the net of control points  $q_{k,l}$ . Then the NUBS surface interpolation can be written as



$$P_{i,j} = \sum_{k=0}^{\nu-1} N_{k,\mu}(u_i) \sum_{l=0}^{nv-1} N_{l,mv}(v_j) q_{k,l} \equiv \sum_{k=0}^{\nu-1} N_{k,\mu}(u_i) R_{k,j} \quad (6)$$

$$(i = 0, \dots, npu - 1, \quad j = 0, \dots, npv - 1)$$

Here,  $mu$  and  $mv$  are the order of the spline functions in the  $u$  and  $v$  directions, respectively,  $nu$  and  $nv$  are the number of control points in the  $u$  and  $v$  directions, respectively, and  $npu$  and  $npv$  are the number of points of the  $P_{i,j}$  net in the  $u$  and  $v$  directions, respectively.  $u_i$  and  $v_j$  are the parameters of  $P_{i,j}$ , which is often given as the distance parameter. In Eq. 6,

$R_{k,j} = \sum_{l=0}^{nv-1} N_{l,mv}(v_j) q_{kl}$  is used. Then, if the surface points  $P_{i,j}$  are given, we can calculate the net of control points  $q_{k,l}$  by inversing Eq. 6 in the following manner. First we solve the inverse equation

$$R_{k,j} = \left( \sum_{i=0}^{nu-1} N_{k,mu}(u_i) \right)^{-1} P_{i,j} \quad (7)$$

This equation shows that the calculated  $R_{k,j}$  can be regarded as the control points for the isoparameter  $u$  line, especially in this study, since it corresponds to each set of control points along the girth line, and this process can be skipped. Next we solve the inverse equation

$$q_{k,j} = \left( \sum_{l=0}^{nv-1} N_{l,mv}(v_j) \right)^{-1} R_{k,j} \quad (8)$$

Then the surface net of control points can be evaluated. However, in order to use the above method, we need to adjust the number of control points for each girth line. In the present method, we newly interpolate

$(N+1) \times nc$  (*peak*) control points for each girth line using the control points calculated with the above-mentioned process (Eqs. 1,3–5). After attaining the net of control points, the hull surface interpolation can be carried out by calculating Eq. 6.

### III. SHIPFLOW ANALYSIS

#### A. About SHIPFLOW

Applications of computational fluid dynamics(CFD) to the maritime industry continue to grow as this advanced technology takes advantage of the increasing speed of computers. Numerical approaches have evolved to a level of accuracy which allows them to be used during the design process to predict ship resistance. Significant progress has been made in predicting flow characteristics around a given ship hull. Ship designers can use this information to improve a ship's design. However, not much effort has been dedicated to determining viscous drag, an important element in the development of a new design. The final checking and analysis of the bulb design is done in the CFD module SHIPFLOW. The wave making and frictional resistance as well as the flow round the hull for various bulb shapes have been calculated using SHIPFLOW. The flow around a body can be described mathematically as a function of fluid pressure and the three components of velocity. A set of governing equations of motions can be created, like the Navier–Stokes equations for turbulent flow, and solved in association with specific boundary condition. These equations are often complex to solve and rely on the use of Computational Fluid Dynamics (CFD). SHIPFLOW is a CFD tool specifically developed to solve marine related problems (SHIPFLOW, 1999). To investigate the flow around a ship or ship model, SHIPFLOW splits the flow into three regions, shown in Figure below: the region of potential flow, which neglects viscous effects and is associated with the wave-making pattern, the region of boundary-layer flow and the region where the complete Navier–Stokes equations are solved.

In CFD analyses of marine vehicles, it is customary to use  $i$ ,  $j$  and  $k$  to describe the grid dimensions, where  $i$ -direction is in the axial direction,  $j$  is

normal to the body, and  $k$  is around the body's girth

The following potential flow techniques are used in Zone 1 to predict pressures, velocities and streamlines. By assuming non-viscous (ideal) and irrotational flow the governing equations produced are the linear, partial differential Laplace equations based on mass continuity. The non-linear free-surface boundary conditions are linearised and solved by using an iterative process until satisfactory convergence is reached.

In Zone w the development of the boundary layer is investigated using momentum integral equations for the thin viscous layer along the hull. By ignoring cross flow in the boundary layer, which is created due to a pressure gradient in the vertical direction of the ship hull the results are ordinary differential equations which are solved by Runge-Kutta techniques. The prediction cannot be used at the stern of a ship where a thick viscous region occurs due to convergence of the streamlines. Towards the stern of the vessel, Reynolds-averaged Navier-Stokes(RANS) equations along with mass continuity equations describe the flow in Zone 3. The solution of the complex Navier-Stokes equations requires a lot of computational time and is therefore restricted to the stern of the vessel only, where a denser panelization is created. The unsteadiness of the turbulent region is averaged out and instantaneous values of pressure and velocity are separated into a mean with fluctuations by the introduction of Reynolds stresses.

The programming is split into six modules and SHIPFLOW considers each module do no affect, for example, the second module. These six modules are listed below, in the order in which SHIPFLOW assesses them

## 1. XFLOW

Defines the general physical properties of the surroundings, for examples the fluid, characteristics, initial ship position, ship speed, etc.

## 2. XMESH

Using the information from XFLOW, XMESH generates the panelization of the free surface and the vessel for use by the third module XPAN. The model can be viewed in the post processor.

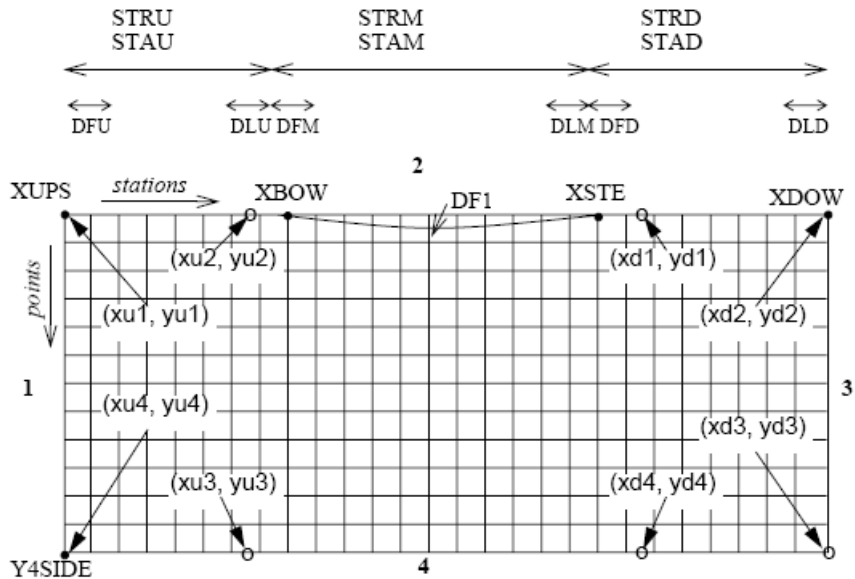


Fig. 5. XMESH

## 3. XPAN

XPAN computes the potential flow around the model (i.e. Zone 1) and free-surface, which are made up of quadrilateral panels each containing Rankine sources. XPAN can operate under linear or non-linear free-surface boundary conditions. Results obtained from XPAN are displayed by the post processor and listed in output files. The results include wave making coefficient ( $C_w$ ), wave pattern, potential streamlines, pressure and velocity contours.

#### 4. XBOUND

XBOUND is concerned with the thin turbulent boundary layer surrounding the hull (i.e. Zone 2). Using momentum integral equations SHIPFLOW provides the frictional resistance coefficient ( $C_f$ ), boundary layer thickness, as well as other parameters associated with the boundary layer.

#### 5. XGRID

XGRID generates the grid towards the stern of the vessel used to represent Zone 3 where the Navier–Stokes equations describe the fluid flow.

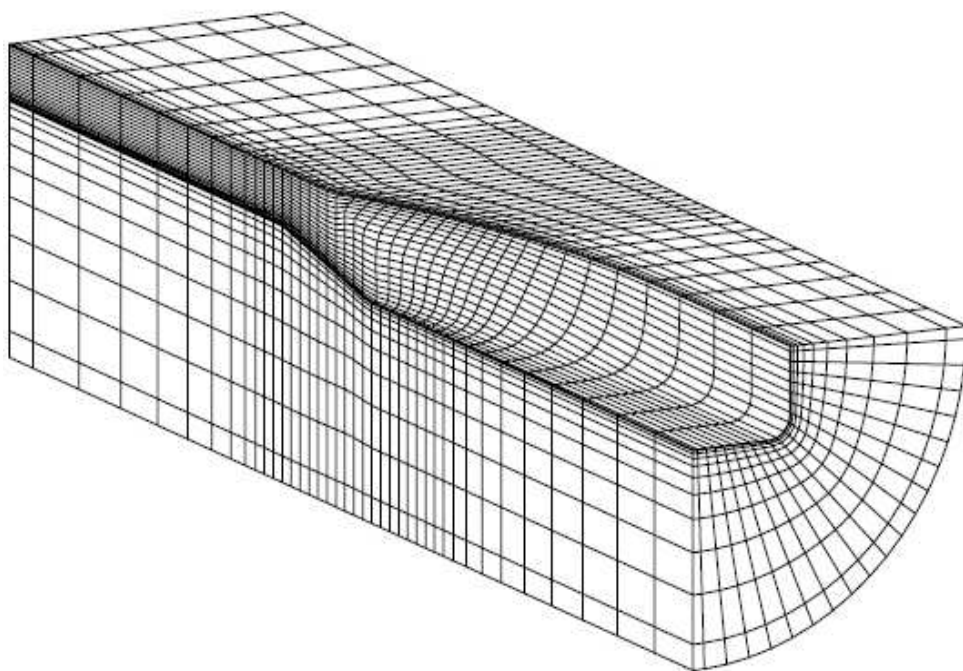


Fig. 6 Grid surrounding the aft half

## 6. XVISC

The final module of SHIPFLOW solves the Reynolds-averaged Navier-stokes equations. XVISC provides the viscous pressure resistance coefficient ( $C_{vp}$ ) and therefore the total resistance  $C_t$  can be estimated. XVISC can also be used to investigate the wake and values such as axial, radial and tangential velocities at various planes towards the stern are obtained. The frictional, wave and total resistance coefficients as computed by SHIPFLOW, together with the total resistance as measured from the experiments and the Schoenherr and ITTC ship model correlation lines.

## IV. THE INVERSE DESIGN PROBLEM

For the inverse problem, the hull form is regarded as being unknown and controlled by a set of control points, in addition, the desired distribution of dimensionless pressure coefficients  $C_{p_i}$  on the hull surface are considered available.

Let the desired pressure coefficients the hull surface be denoted by  $C_p(x, y_i, z) \equiv C_{p_i}, i = 1$  to  $l$ , where  $l$  represents the number of panel for the redesign portion of hull. Then the inverse problem can be stated as follows: by utilizing the above mentioned desired pressure coefficients  $C_{p_i}$ , design the new hull shape.

The solution of the present inverse design problem is to be obtained in such a way that the following functional is minimized:

$$J[\hat{\Omega}(\hat{B})] = \sum_{i=1}^I [\hat{C}_{p_i}(\hat{B}_j) - C_{p_i}]^2 = U^T U ; \quad j = 1 \text{ to } J \quad (9)$$

here,  $\hat{C}_{p_i}$  are the estimated or computed pressure coefficients on the hull

locations  $(x, y_i, z)$ . These quantities are determined from the solution of the direct problem given previously by using an estimated hull form  $\hat{\Omega}(\hat{B})$ ,  $J$  represents the number of control points, i.e.  $J = (n+1) \times (m+1)$ . Here the hat " ^ " denotes the estimated quantities.

#### A. The Levenberg–Marquardt method for minimization

If the redesigned hull shape is discretized into  $l$  panels and  $J$  control points are used, Eq. 10 is minimized with respect to the estimated parameters  $B_j$  to obtain

$$J[\hat{\Omega}(\hat{B})]/\partial B_j = \sum_{i=1}^I \left[ \frac{\partial \hat{C}p_i}{\partial B_j} \right] [\hat{C}p_i - C p_i] = 0 ; j = 1 \text{ to } J \quad (10)$$

where should be equal to or greater than  $J$ , otherwise an under determined system of equations will be obtained and it is impossible to calculate the inverse solutions under this situation. Eq. 11 is linearized by expanding  $\hat{C}p_i(B_j)$  in Taylor series and retaining the first order terms. Then a damping parameter  $\mu$  is added to the resulting expression to improve convergence, leading to the Levenberg–Marquardt method (Marquardt 1963) given by

$$(F + \mu^n I) \Delta B = D \quad (11a)$$

where

$$F = \psi^T \psi \quad (11b)$$

$$D = \psi^T U \quad (11c)$$

$$\Delta B = B^{n+1} - \quad (11d)$$



here the superscript  $n$  and  $T$  represent the iteration index and transport matrix, respectively,  $I$  is the identity matrix and  $\psi$  denotes the Jacobian matrix defined as

$$\psi \equiv \frac{\partial Cp}{\partial B^T} \quad (12a)$$

Eq. 11a is now written in a form suitable for iterative calculation as

$$B^{n+1} = B^n + (\psi^T \psi + \mu^n I)^{-1} \psi^T (\widehat{Cp} - Cp) \quad (12b)$$

When  $\mu^n = 0$ , the Newton's method is obtained, as  $\mu^n \rightarrow \infty$ , the steepest-descent method is obtained. For fast convergence the steepest-descent method is applied first, then the value of  $\mu^n$  is decreased, finally the Newton's method is used to obtain the inverse solution. The algorithm of choosing this damping value  $\mu^n$  is described in detailed in (Marquardt 1963).

## V. EXAMPLES

### A. EXAMPLE 1.

#### – SERIES 60

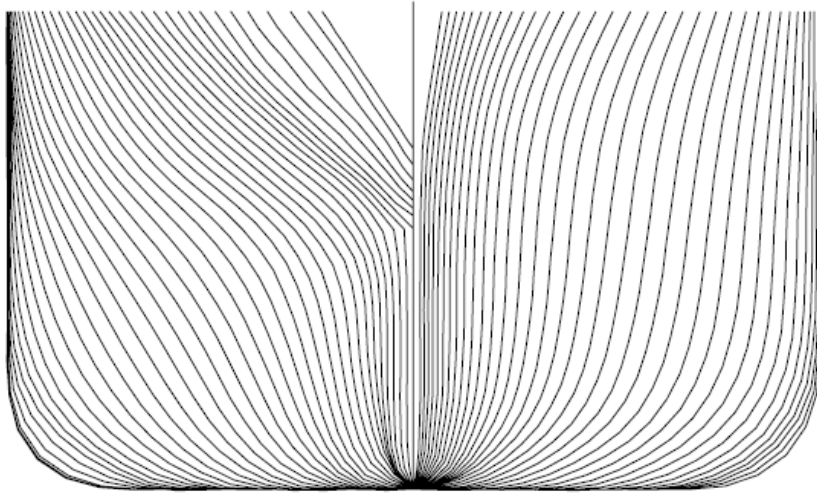


Fig. 7 Body plan of Series 60

In the first example, the parent ship is a series-60 ship and is shown in Figure 5. The Froude number  $Fr$  is taken as 0.316 and  $C_b$  is 0.6.

The pressure distribution can thus be calculated and used as the design criterion. Fig. 8 ~ 11 shows the contour plot of pressure coefficient ( $C_p$ ) of Series 60.

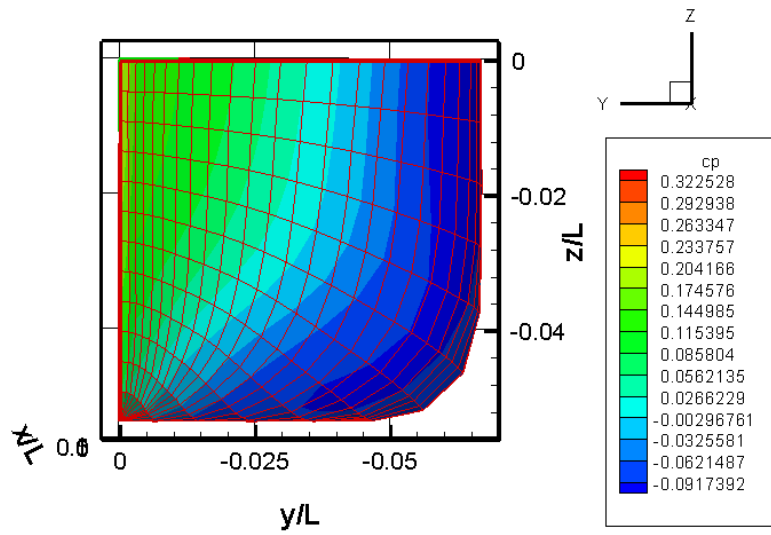


Fig. 8 Cp value of series 60 original. Stemview

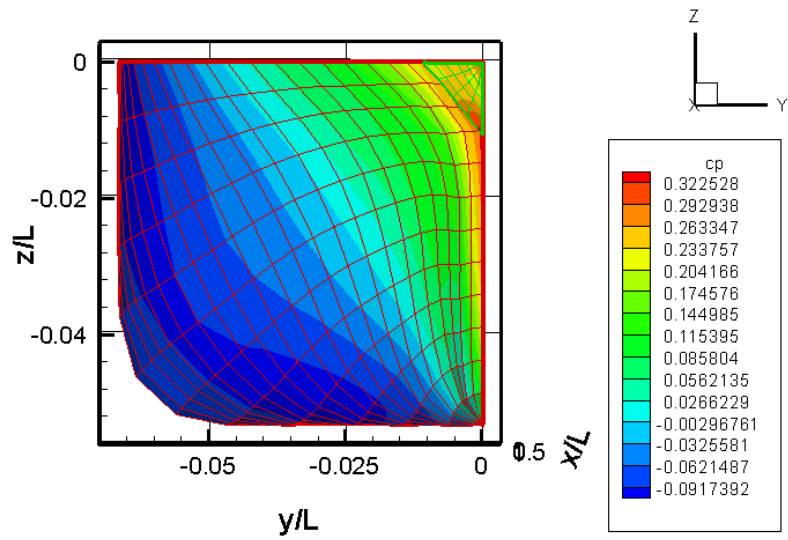


Fig. 9 Cp value of series 60 original. Stern view

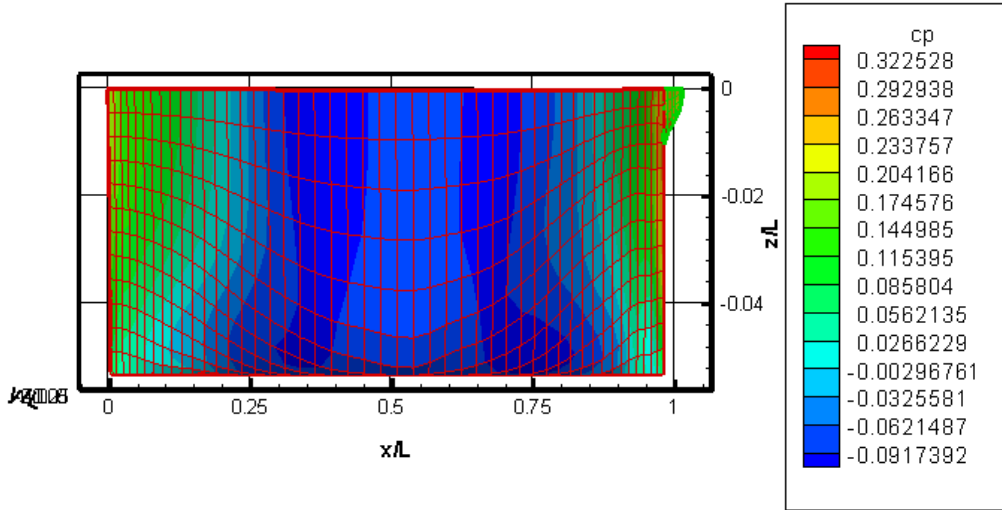


Fig. 10  $C_p$  value of series 60 original. Sideview

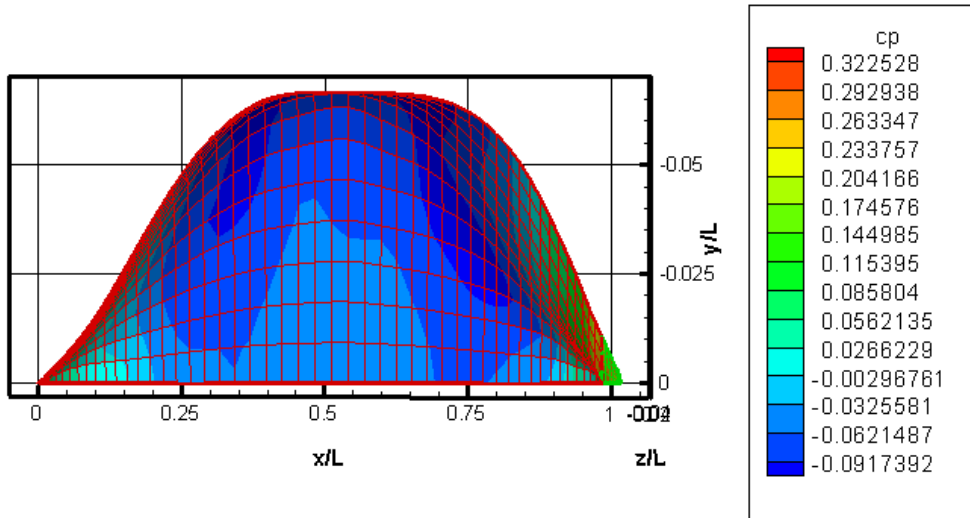


Fig. 11  $C_p$  value of series 60 original. Bottom view

The inverse calculations are then performed by following the Levenberg – Marquardt method (LMM). The initial guesses of  $B_j$  are obtained by using Fourier NUBS surface fitting for the parent ship. With only 4 iterations a very accurate solution can be obtained.

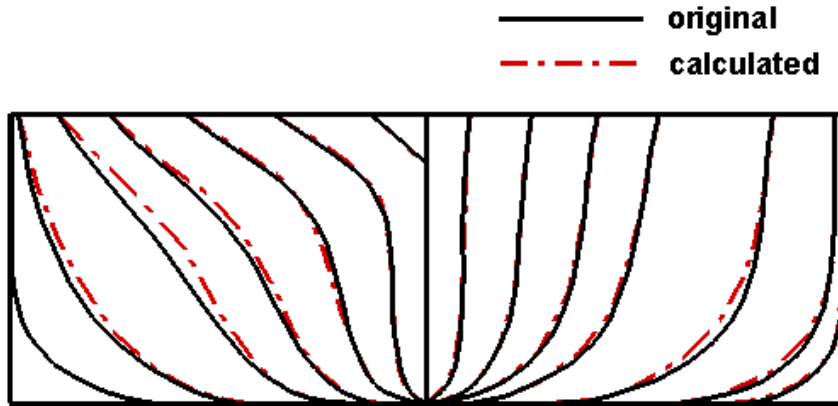


Fig. 12 Comparison of girth lines with original lines

respectively. From Fig. 12, conclude that the Levenberg – Marquardt method has been applied successfully in estimating the optimal hull form in this numerical example.

In order to show the natural of generality for the Levenberg – Marquardt method in the optimization problem, we will perform another numerical experiment.

## B. EXAMPLE 2

– KCS (KRISO CONTAINERSHIP 3600TEU)

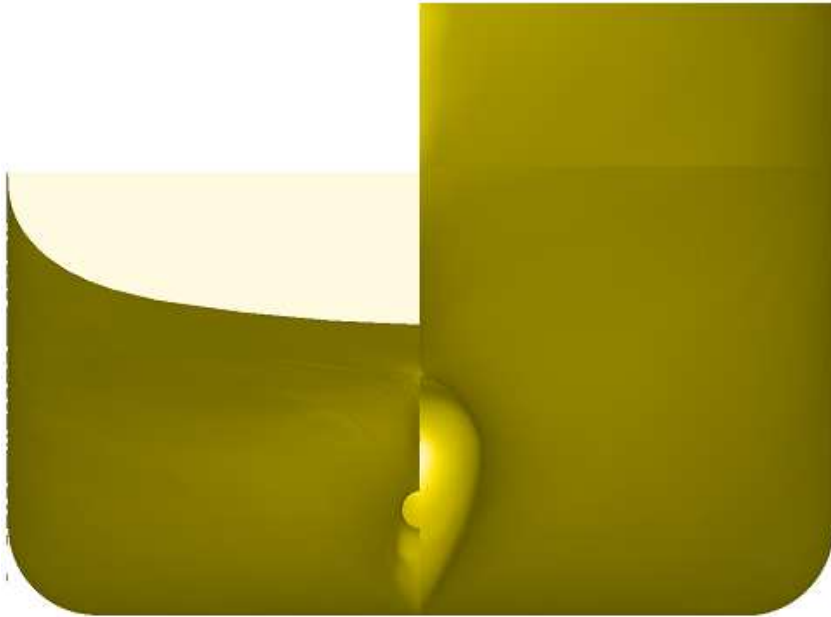


Fig. 13 Front view of KCS

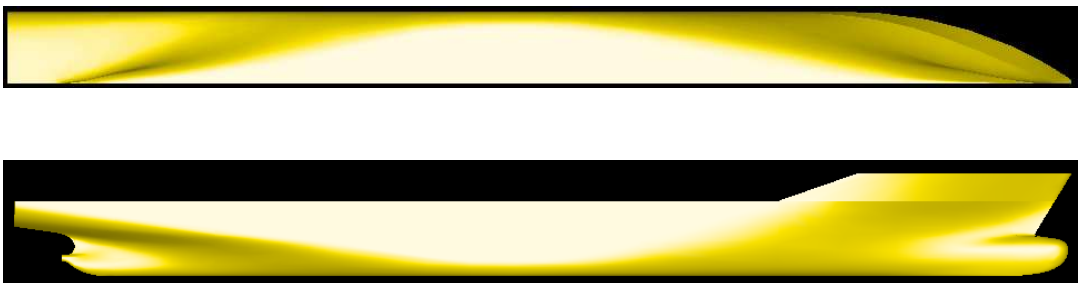


Fig. 14 Bottom (Above) and side (Below) view of KCS

In the second example, the parent ship is a container ship and is shown in Fig. 13 ~ 14. The whole ship is divided into four blocks and the first block is the bow. The Froude number  $Fr$  is taken as 0.2599 and the principle particulars of KCS Model test model is as shown in Table 1.

Table 1 The principle particulars of KCS

	Ship	Model
Scale ratio	1.0	1/31.6
Speed (m/s)	12.3467	2.1964
Fn	0.26	0.26
Re	$2.4 \times 10^9$	$1.4 \times 10^7$
Lpp (m)	230.0	7.2786
B (m)	32.2	1.0190
D (m)	19.0	0.6013
T (m)	10.8	0.3418
S (m <sup>2</sup> )	9,498.0	9.5121
Displacement (m <sup>3</sup> )	52,030.0	1.6490
CB	0.6505	0.6505

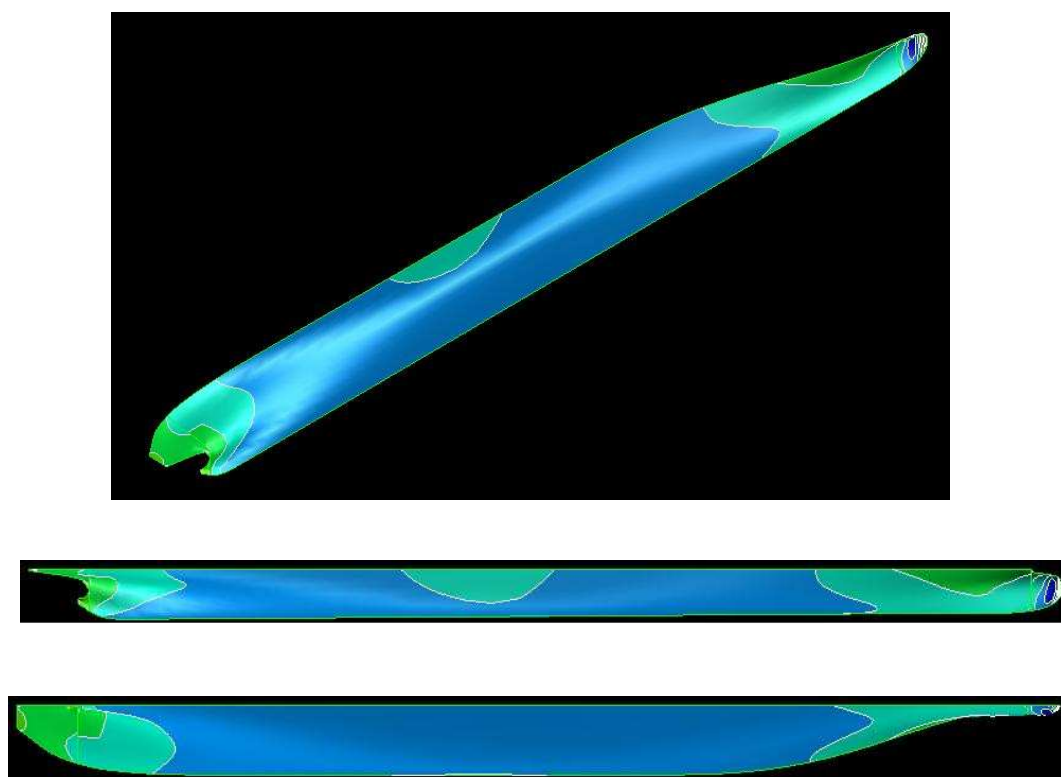


Fig. 15 Cp values of KCS.

The reason why the contour plot of  $C_p$  becomes denser within the hull form region for the exact ship is the same as that stated in example 1.

The inverse calculations are performed again by using the Levenberg–Marquardt method (LMM). The initial guesses of  $B_j$  are obtained by using Fourier NUBS surface fitting for the parent ship. After only 4 iterations a very accurate solution can be obtained.

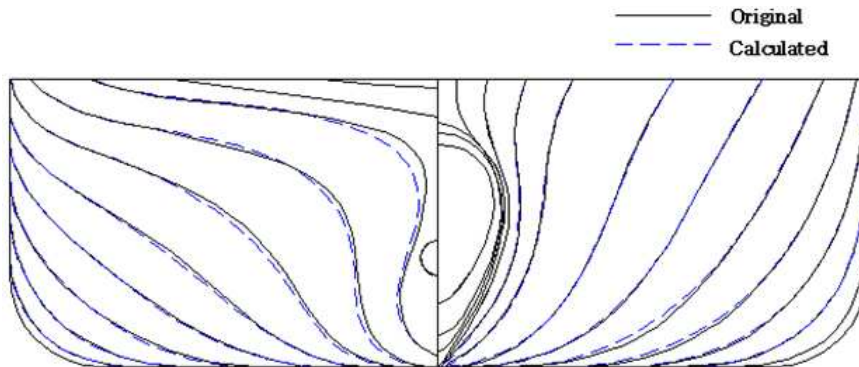


Fig. 16 Comparison of body plans for Original and Calculated hull form

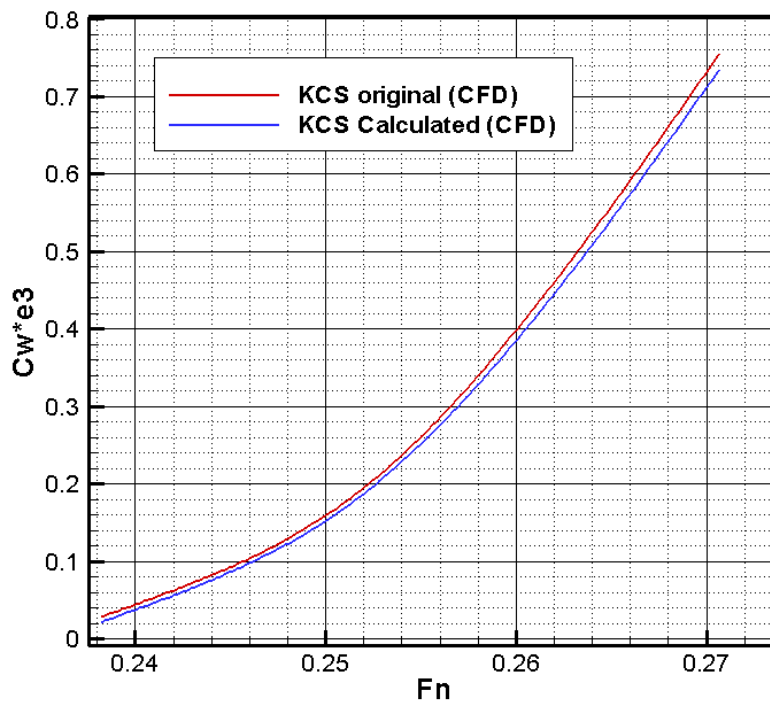


Fig. 17 Comparison of  $C_w$  for Original and Calculated hull form



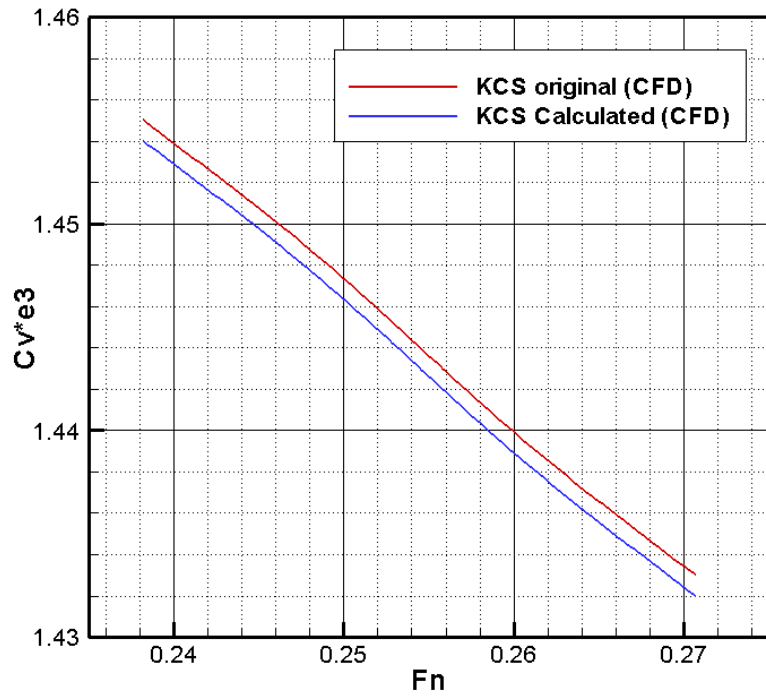


Fig. 18 Comparison of  $C_v$  for Original and Calculated hull form

From Fig. 17 ~ 18 and Appendix 2, conclude again that the Levenberg–Marquardt method has been applied successfully in estimating the optimal hull form in this numerical example.

## VI. CONCLUSIONS

An inverse design problem in estimating the optimal hull form from the knowledge of desired pressure distribution by the techniques of Fourier NUBS surface fitting and Levenberg–Marquardt method has been developed and applied successfully.

Results show that the present algorithm needs only a few iterations to obtain the optimal hull form if enough number of control points are given. One should note that even though more control points describe the unknown surface more accurately, on the other hand, it takes more computer time to obtain the inverse solutions.

The advantages of using the technique of inverse design problem in designing the optimal hull form line is that distorting the parent hull form by changing the control points to obtain an exact (or desired) hull form, the time needed in fundamental design can be shortened and calculate the pressure distribution for the exact hull form and retain the pressure distribution around bow as the desired pressure distribution  $C_p$ , the cost for model test can be reduced.

## Reference

- 1.Huang, C.H. and Huang, M. C. (1994) "Inverse Problem in Determining the Normal and Tangential Drag Coefficients of Marine Cables" J of Ship Research,38,296-301.
- 2.keun Jae Kim, "SHIPFLOW calculations and resistance minimization"  
Dr thesis
- 3.Larsson, L., Kim, K. J., Esping, B. and Holm, D. (1992)  
"Hydrodynamic Optimization using Ship flow. In Practical Design of Ships and Mobile Units. J. B. Caldwell and G. Ward, Eds." Elsevier Applied Science, London, 1.1-1.16.
- 4.Ragab S.A. (2001) "An adjoint formulation for shape optimization in free-surface potential flow." J of Ship Research 45:269-278

## **APPENDIXES**

APPENDIX 1 The Flow characteristics around the Series 60

APPENDIX 2 Comparison of flow characteristics around the KCS, New KCS

# TABLE OF FIGURES

## APPENDIX 1 Series 60

Fig. 1 Wave profile and Wave pattern of KCS (Above) and New KCS (Below) at $Fn$ 0.316	...	2
Fig. 2 Grid for Series 60	...	2
Fig. 3 Dynamic Pressure Coefficient for Series 60 at Station 3 ( $x=0.85$ )	...	3
Fig. 4 Dynamic Pressure Coefficient for Series 60 at Station 2 ( $x=0.9$ )	...	3
Fig. 5 Dynamic Pressure Coefficient for Series 60 at Station 1 ( $x=0.95$ )	...	4
Fig. 6 Dynamic Pressure Coefficient for Series 60 at AP ( $x=1.0$ )	...	4
Fig. 7 Velocity vectors for Series 60 at Station 3 ( $x=0.85$ )	...	5
Fig. 8 Velocity vectors for Series 60 at Station 2 ( $x=0.9$ )	...	5
Fig. 9 Velocity vectors for Series 60 at Station 1 ( $x=0.95$ )	...	6
Fig. 10 Velocity vectors for Series 60 at Station AP ( $x=1.0$ )	...	6
Fig. 11 Turbulence kinetic energy for Series 60 at Station 3 ( $x=0.85$ )	...	7
Fig. 12 Turbulence kinetic energy for Series 60 at Station 2 ( $x=0.9$ )	...	7
Fig. 13 Turbulence kinetic energy for Series 60 at Station 1 ( $x=0.95$ )	...	8
Fig. 14 Turbulence kinetic energy for Series 60 at ( $x=1.0$ )	...	8

## APPENDIX 2 KCS and New KCS

Fig. 15 Comparison of Wave profile and Wave pattern at 20knots	...	10
Fig. 16 Comparison of Wave profile and Wave pattern at 21knots	...	11
Fig. 17 Comparison of Wave profile and Wave pattern at 22knots	...	12
Fig. 18 Comparison of Wave profile and Wave pattern at 23knots	...	13
Fig. 19 Comparison of Wave profile and Wave pattern at 24knots	...	14
Fig. 20 Comparison of Wave profile and Wave pattern at 25knots	...	15
Fig. 21 Comparison of Wave profile and Wave pattern at 26knots	...	16

Fig. 22 Comparison of Dynamic Pressure Coefficient at Station 3 ( $x=0.85$ )	... 17
Fig. 23 Comparison of Dynamic Pressure Coefficient at Station 2 ( $x=0.9$ )	... 18
Fig. 24 Comparison of Dynamic Pressure Coefficient at Station 1 ( $x=0.95$ )	... 19
Fig. 25 Comparison of Dynamic Pressure Coefficient at propeller plane ( $x=0.98625$ )	... 20
Fig. 26 Comparison of Dynamic Pressure Coefficient at AP ( $x=1.0$ )	... 21
Fig. 27 Comparison of Velocity vectors at Station 3 ( $x=0.85$ )	... 22
Fig. 28 Comparison of Velocity vectors at Station 2 ( $x=0.9$ )	... 23
Fig. 29 Comparison of Velocity vectors at Station 1 ( $x=0.95$ )	... 24
Fig. 30 Comparison of Velocity vectors at propeller plane ( $x=0.98625$ )	... 25
Fig. 31 Comparison of Velocity vectors at AP ( $x=1.0$ )	... 26
Fig. 32 Comparison of Turbulence kinetic energy at Station 3 ( $x=0.85$ )	... 27
Fig. 33 Comparison of Turbulence kinetic energy at Station 2 ( $x=0.9$ )	... 28
Fig. 34 Comparison of Turbulence kinetic energy at Station 1 ( $x=0.95$ )	... 29
Fig. 35 Comparison of Turbulence kinetic energy at propeller plane ( $x=0.98625$ )	... 30
Fig. 36 Comparison of Turbulence kinetic energy at AP ( $x=1.0$ )	... 31

## APPENDIX 1

### The Flow characteristics around the Series 60

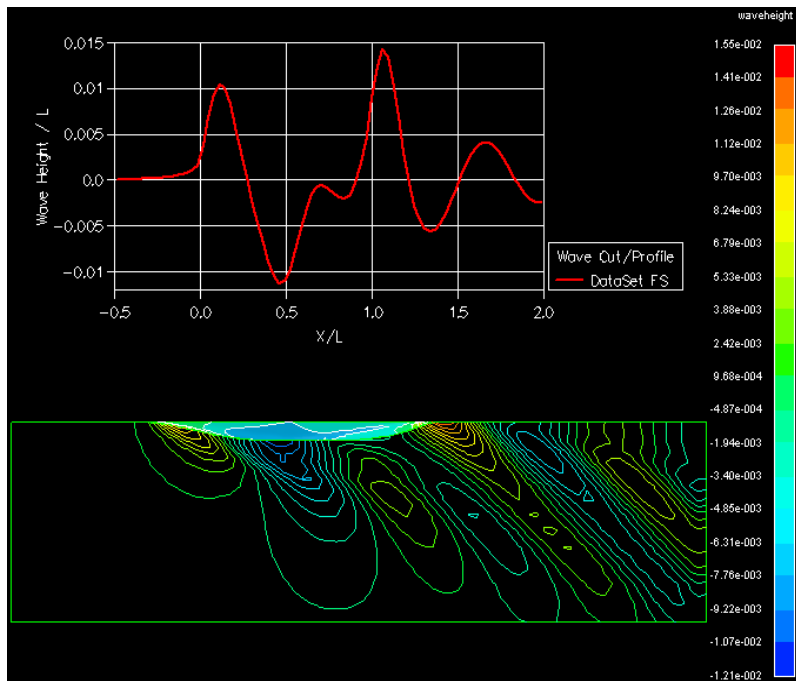


Fig. 1 Wave profile and Wave pattern of KCS (Above) and New KCS (Below) at  $Fn$  0.316

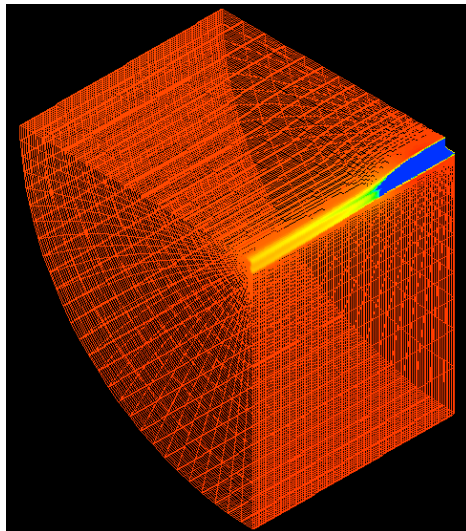


Fig. 2 Grid for Series 60



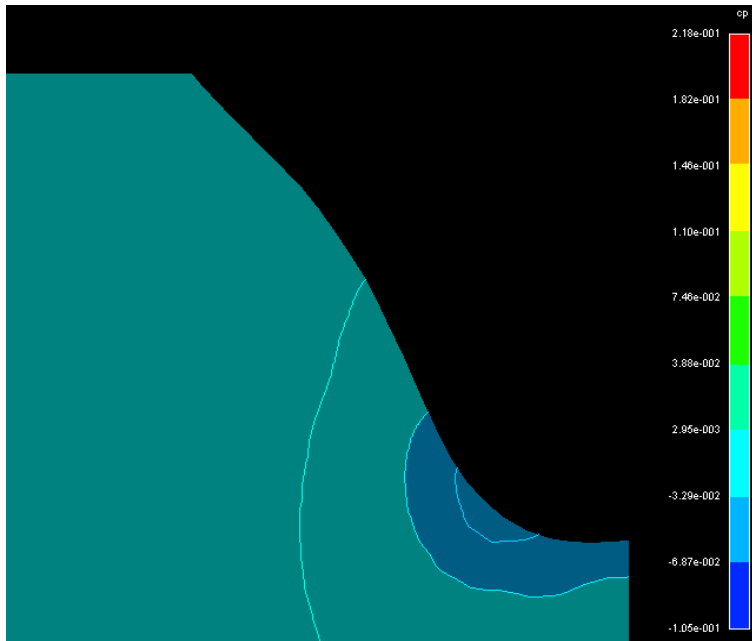


Fig. 3 Dynamic Pressure Coefficient for Series 60 at Station 3 ( $x=0.85$ )

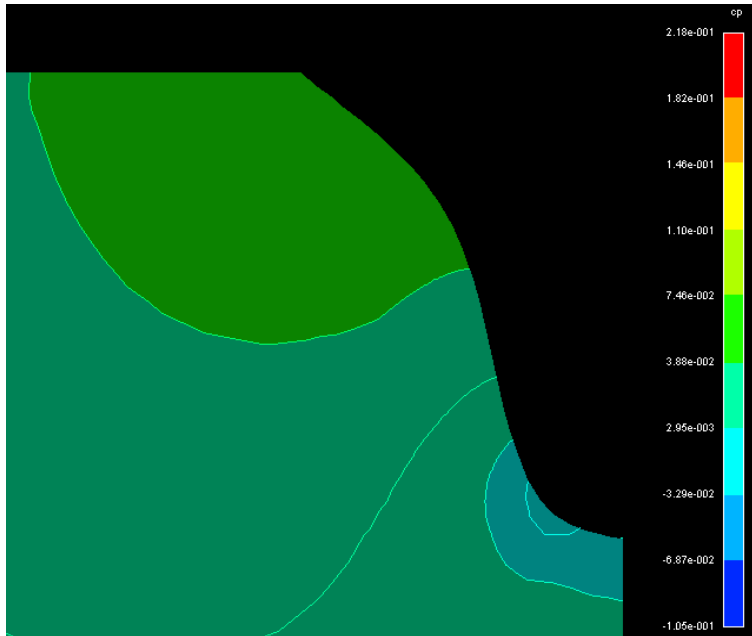


Fig. 4 Dynamic Pressure Coefficient for Series 60 at Station 2 ( $x=0.9$ )

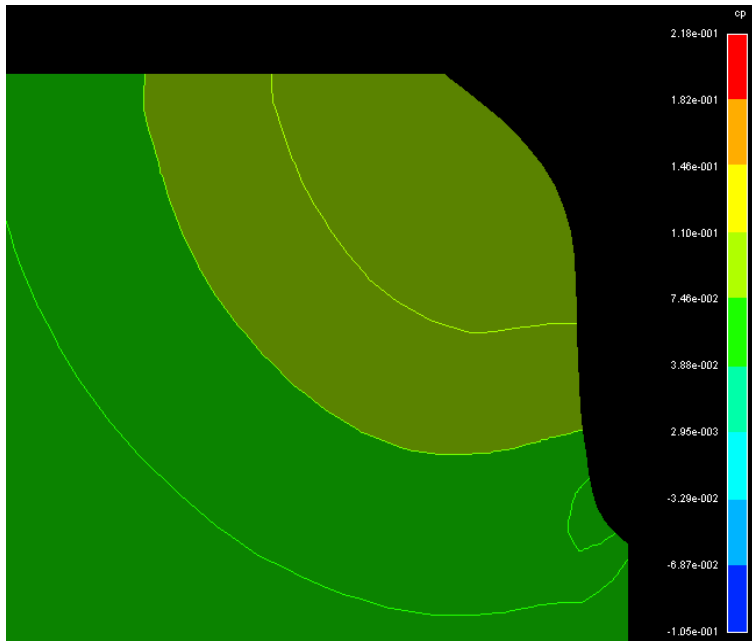


Fig. 5 Dynamic Pressure Coefficient for Series 60 at Station 1 ( $x=0.95$ )

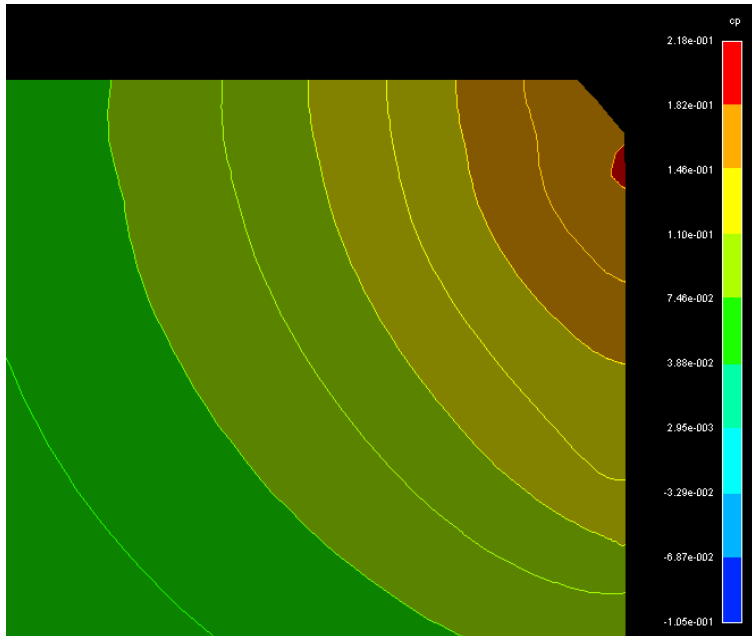


Fig. 6 Dynamic Pressure Coefficient for Series 60 at AP ( $x=1.0$ )

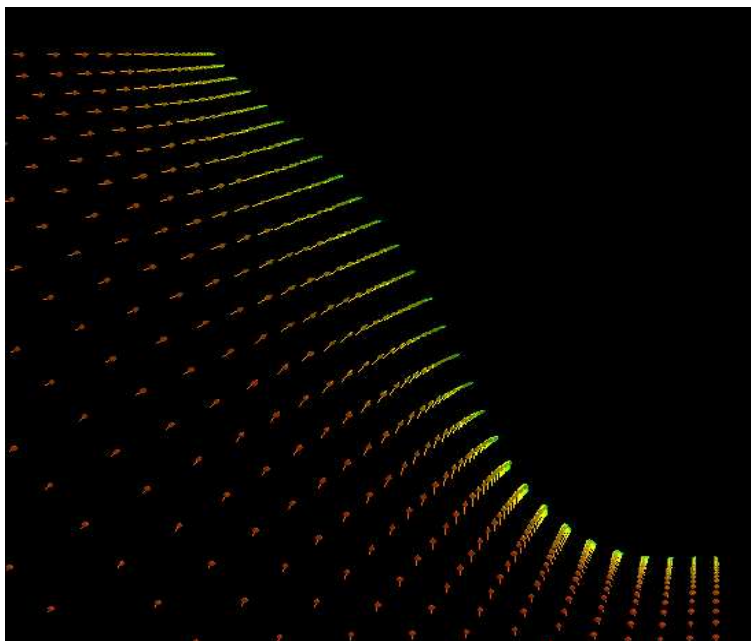


Fig. 7 Velocity vectors for Series 60 at Station 3 ( $x=0.85$ )

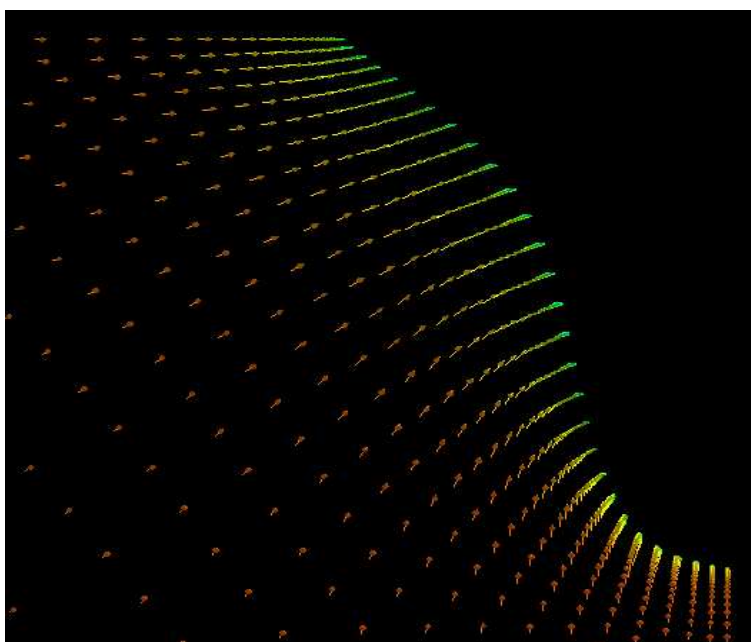


Fig. 8 Velocity vectors for Series 60 at Station 2 ( $x=0.9$ )

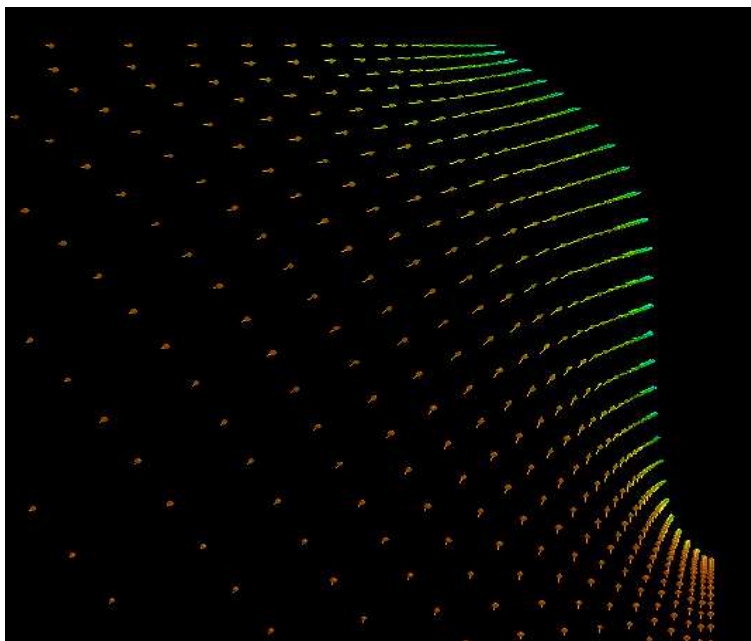


Fig. 9 Velocity vectors for Series 60 at Station 1 ( $x=0.95$ )

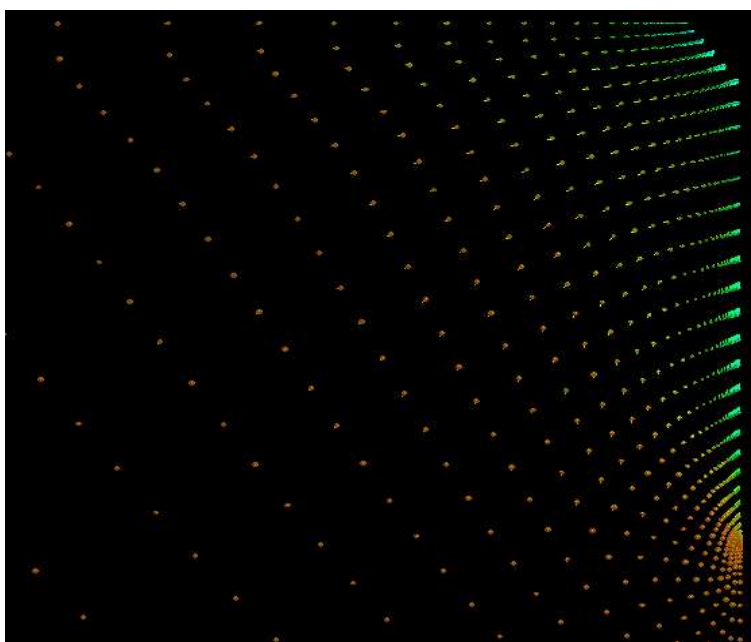


Fig. 10 Velocity vectors for Series 60 at AP ( $x=1.0$ )

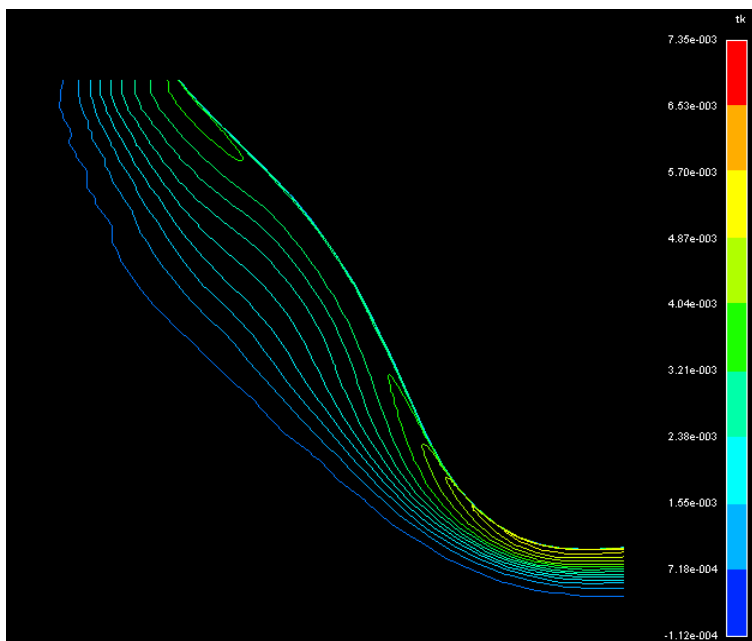


Fig. 11 Turbulence kinetic energy for Series 60 at Station 3 ( $x=0.85$ )

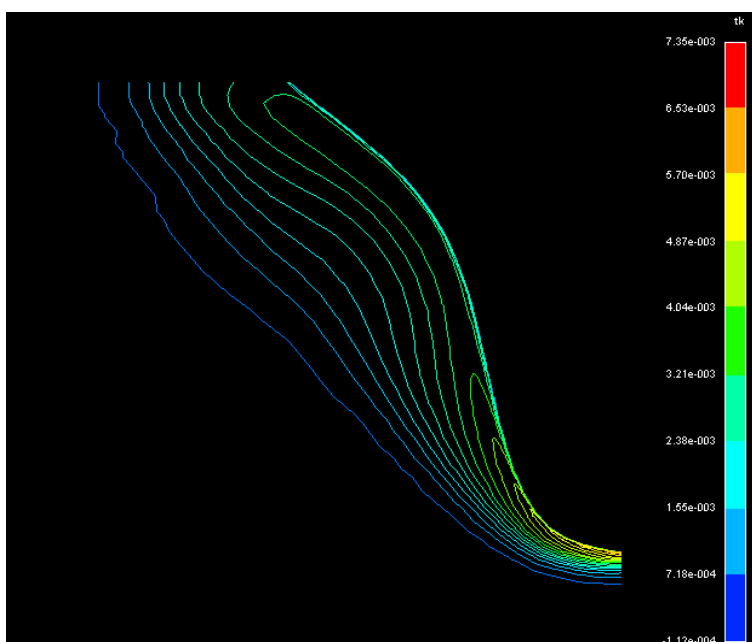


Fig. 12 Turbulence kinetic energy for Series 60 at Station 2 ( $x=0.9$ )

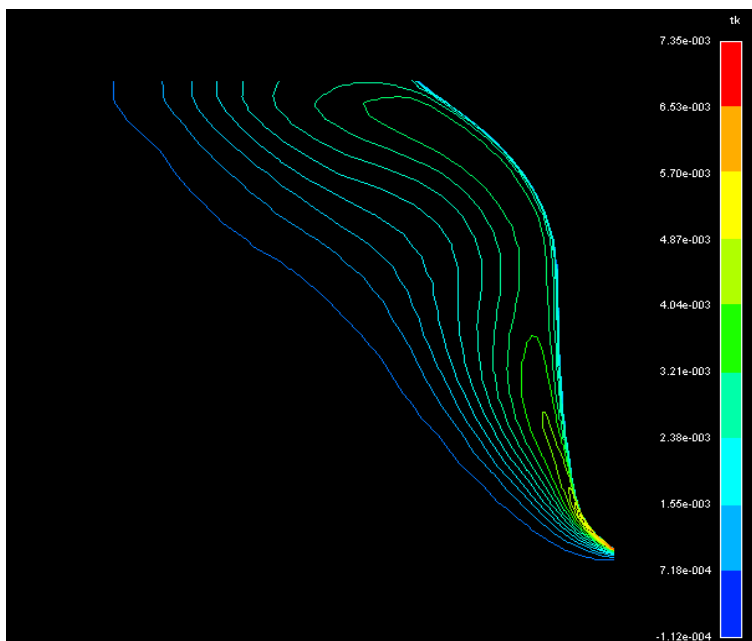


Fig. 13 Turbulence kinetic energy for Series 60 at Station 1 ( $x=0.95$ )

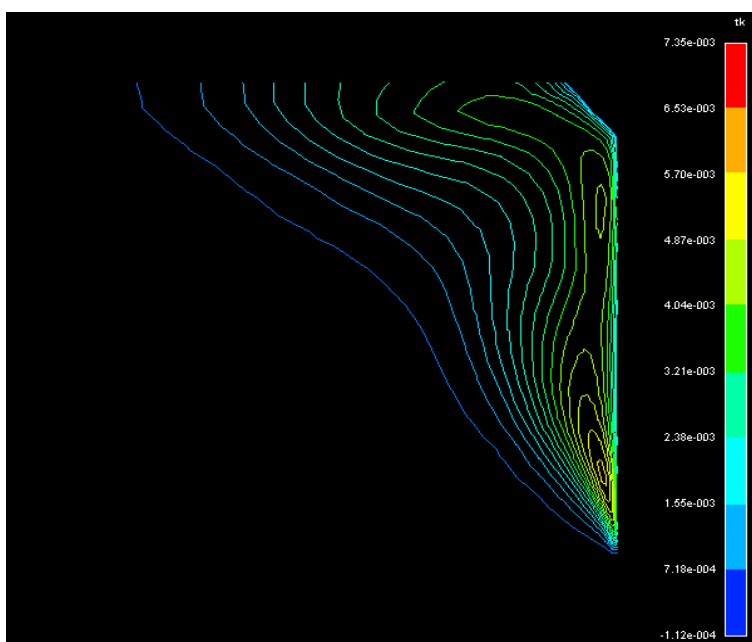
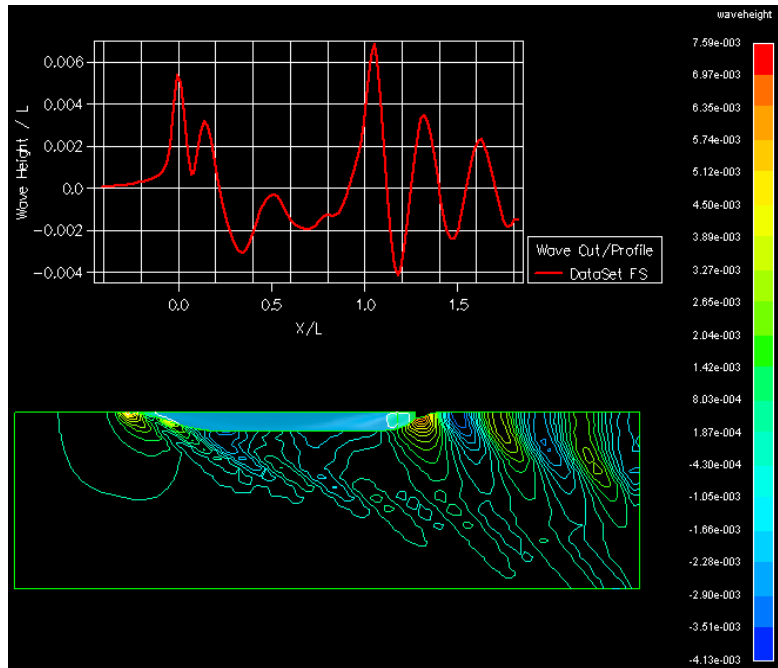


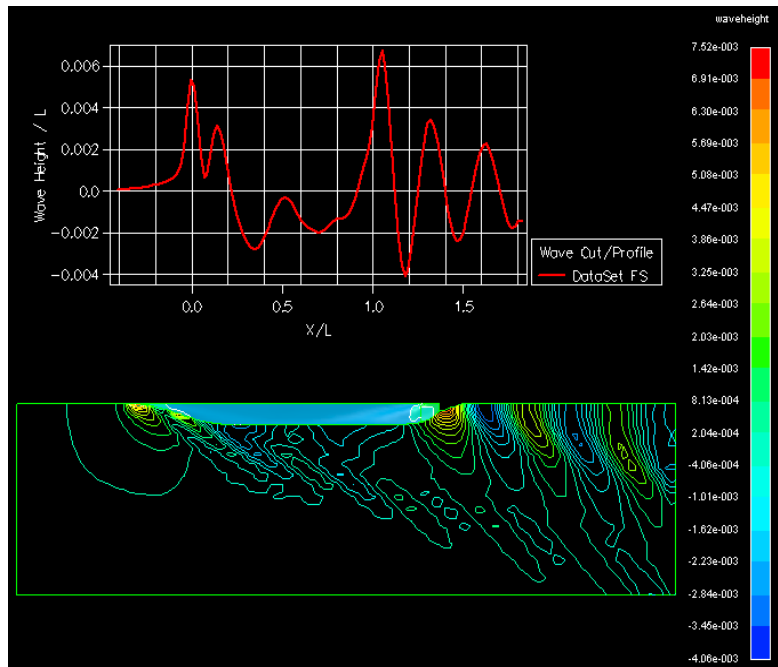
Fig. 14 Turbulence kinetic energy for Series 60 at AP ( $x=1.0$ )

## APPENDIX 2

### Comparison of flow characteristics around the KCS, New KCS



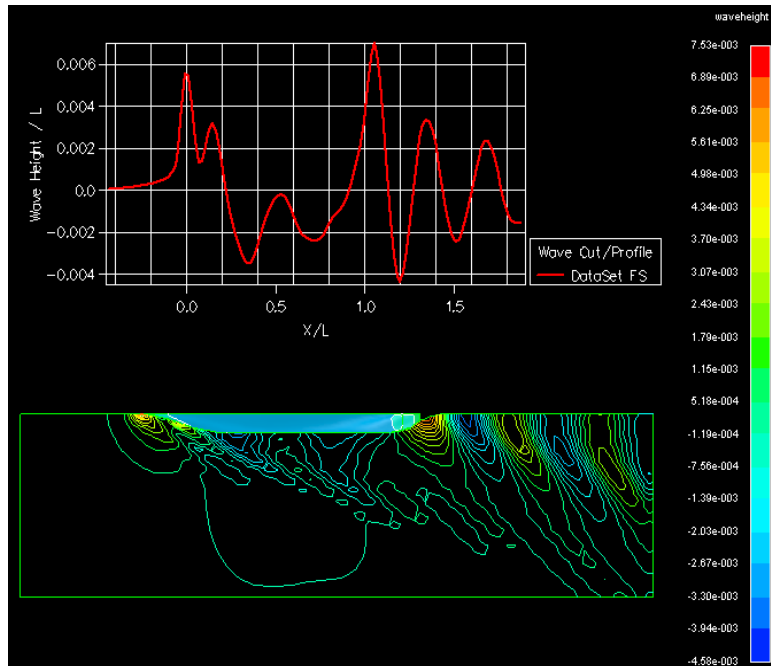
KCS (Original Hull form)



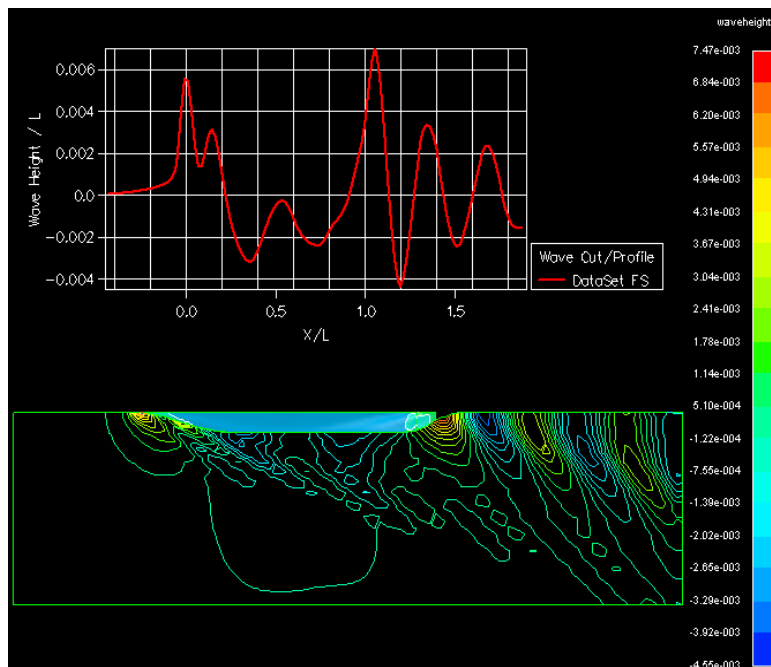
New KCS ( Developed Hull Form)

Fig. 15 Comparison of Wave profile and Wave pattern at 20knots



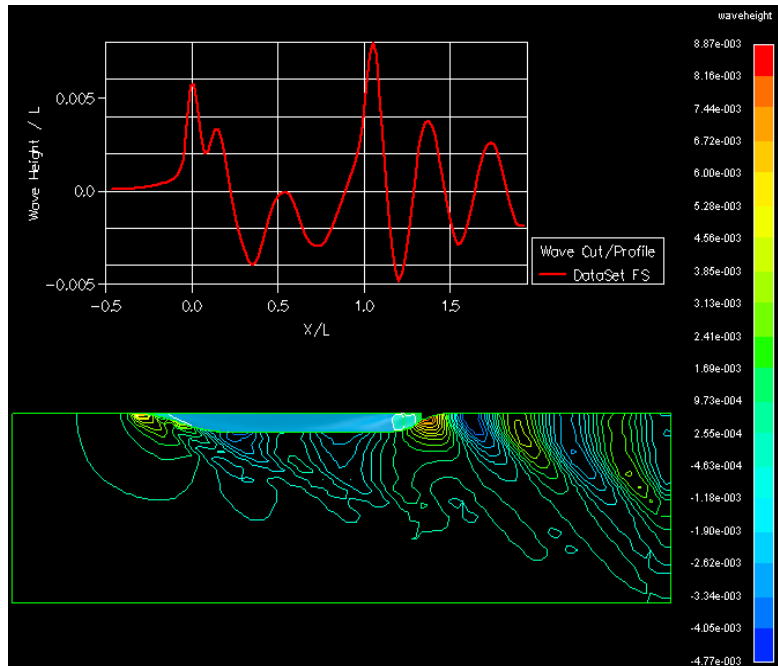


KCS (Original Hull form)

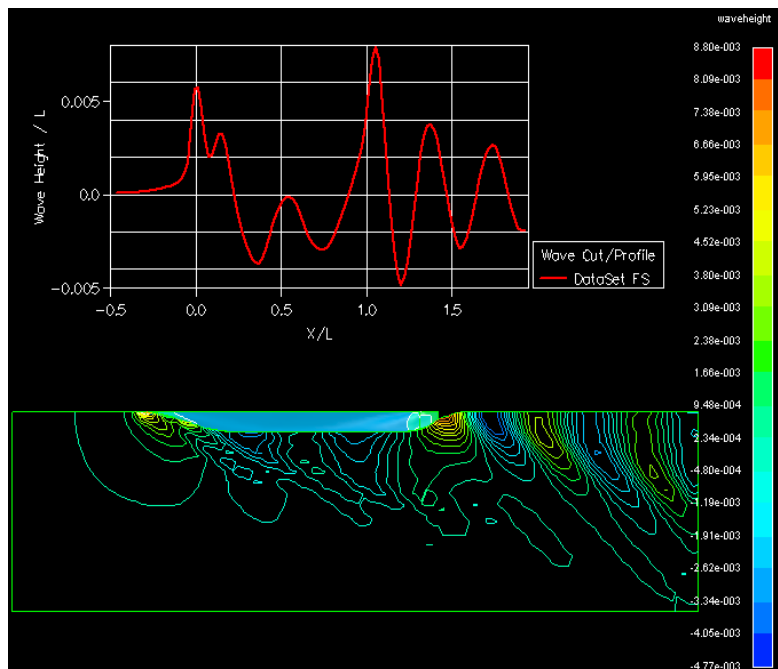


New KCS ( Developed Hull Form)

Fig. 16 Comparison of Wave profile and Wave pattern at 21knots

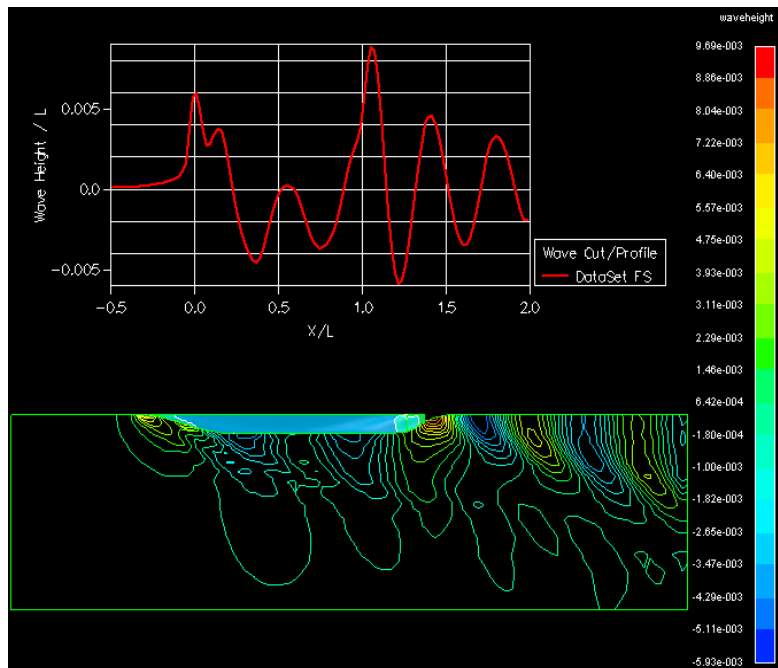


KCS (Original Hull form)

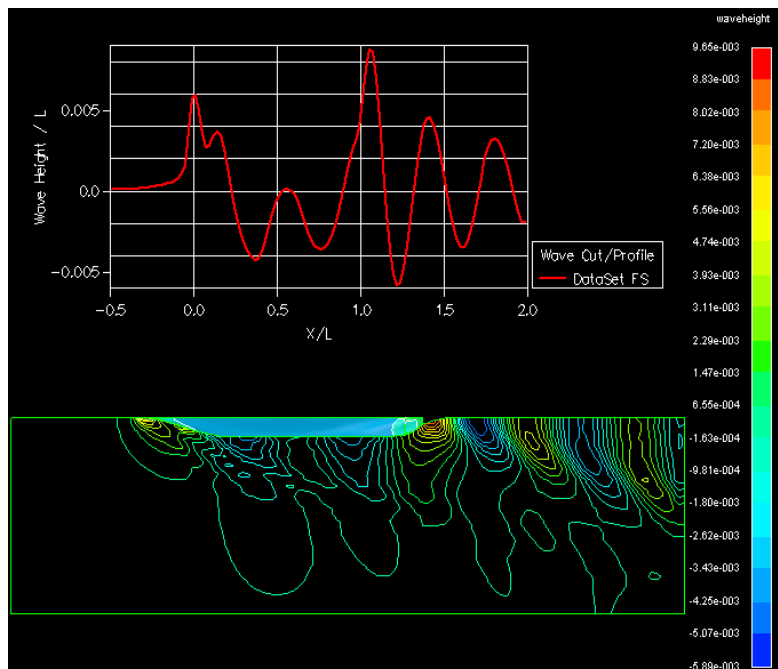


New KCS ( Developed Hull Form)

Fig. 17 Comparison of Wave profile and Wave pattern at 22knots

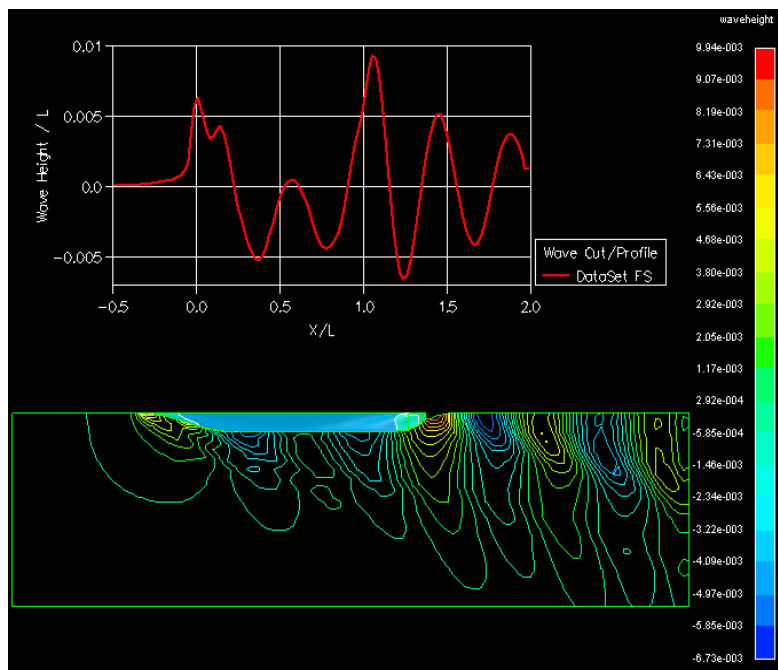


KCS (Original Hull form)

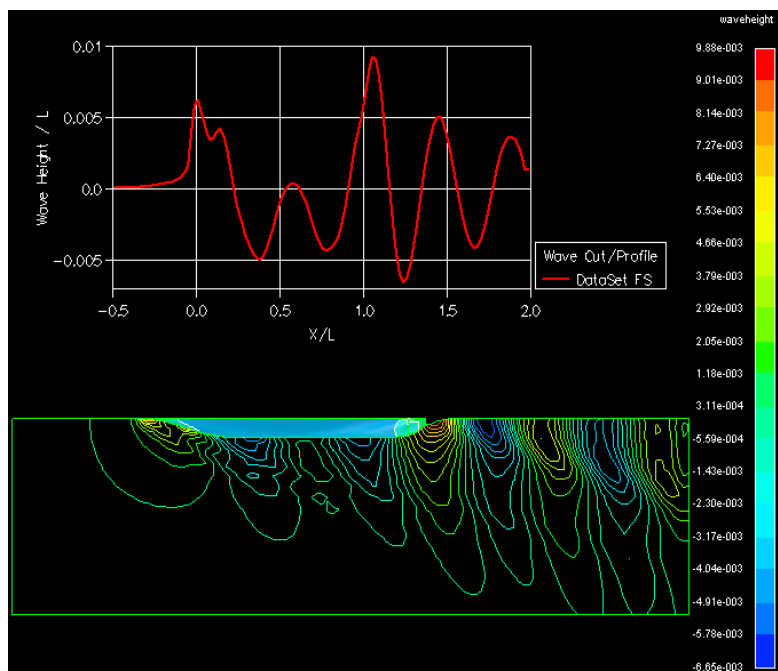


New KCS ( Developed Hull Form)

Fig. 18 Comparison of Wave profile and Wave pattern at 23knots

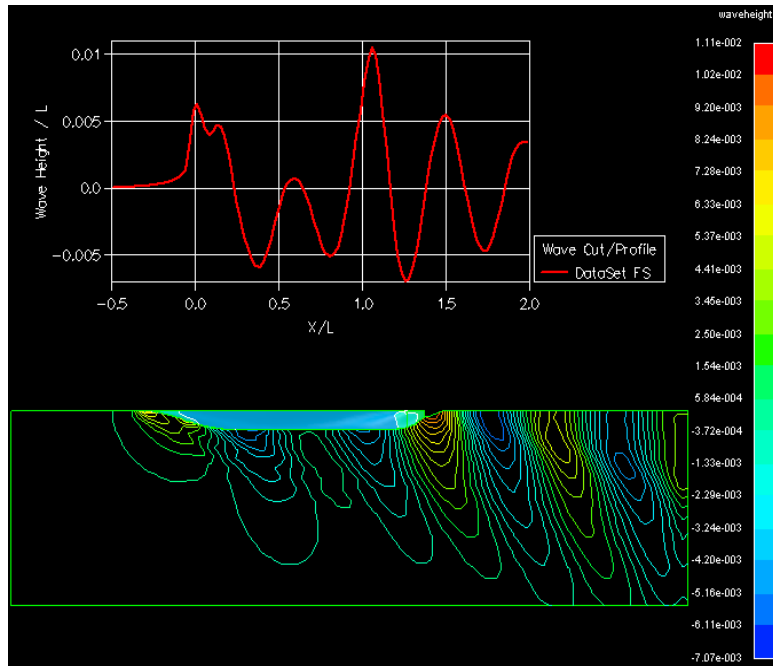


KCS (Original Hull form)

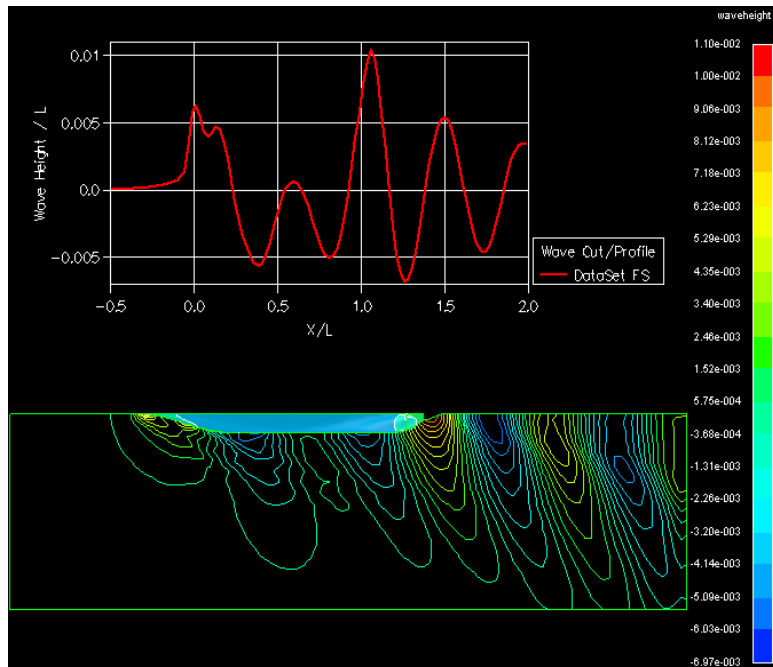


New KCS ( Developed Hull Form)

Fig. 19 Comparison of Wave profile and Wave pattern at 24knots

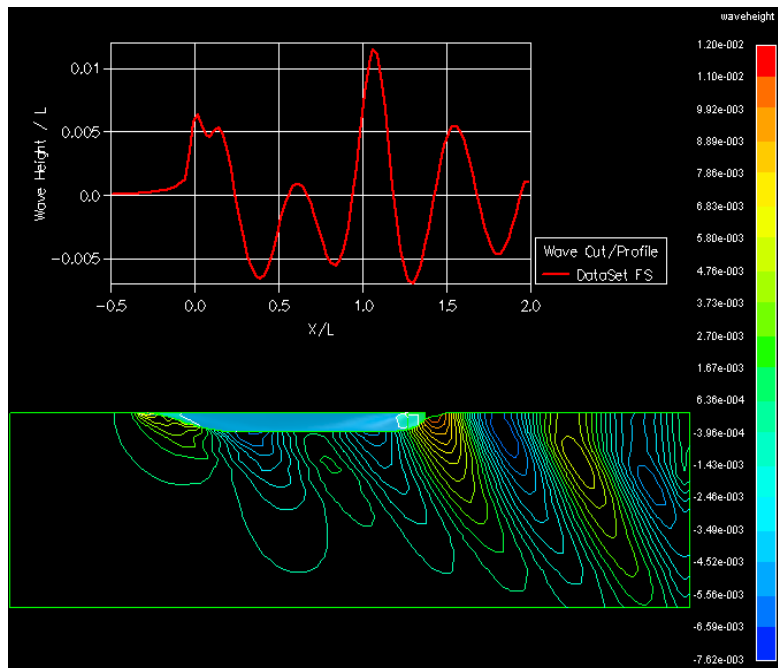


KCS (Original Hull form)

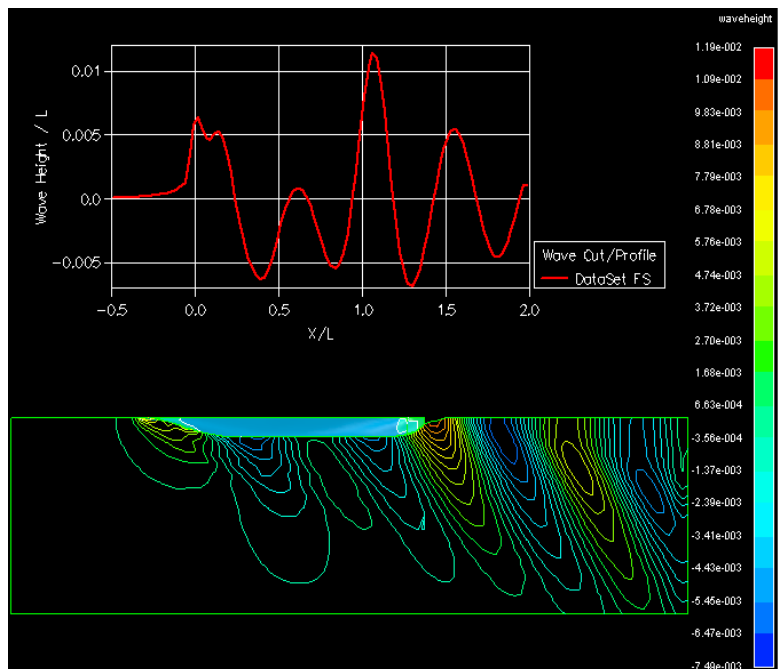


New KCS ( Developed Hull Form)

Fig. 20 Comparison of Wave profile and Wave pattern at 25knots

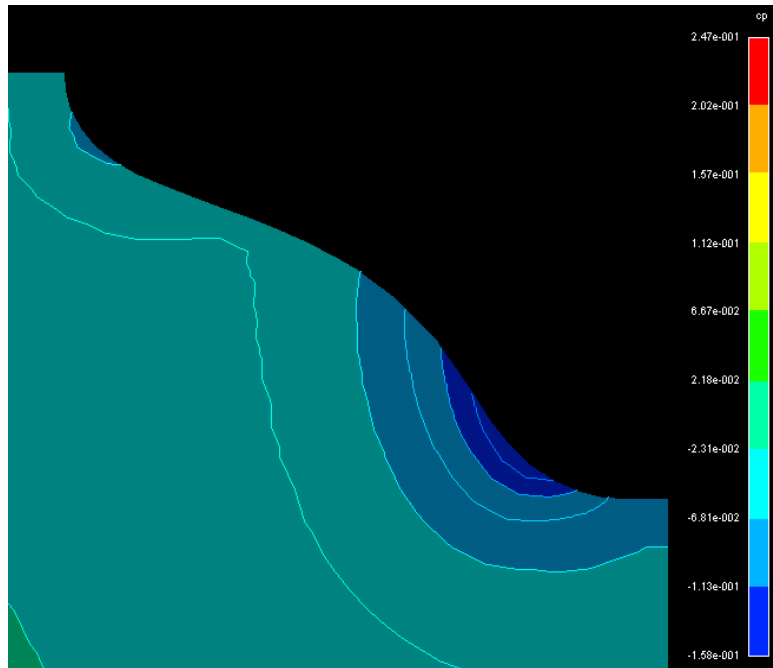


KCS (Original Hull form)

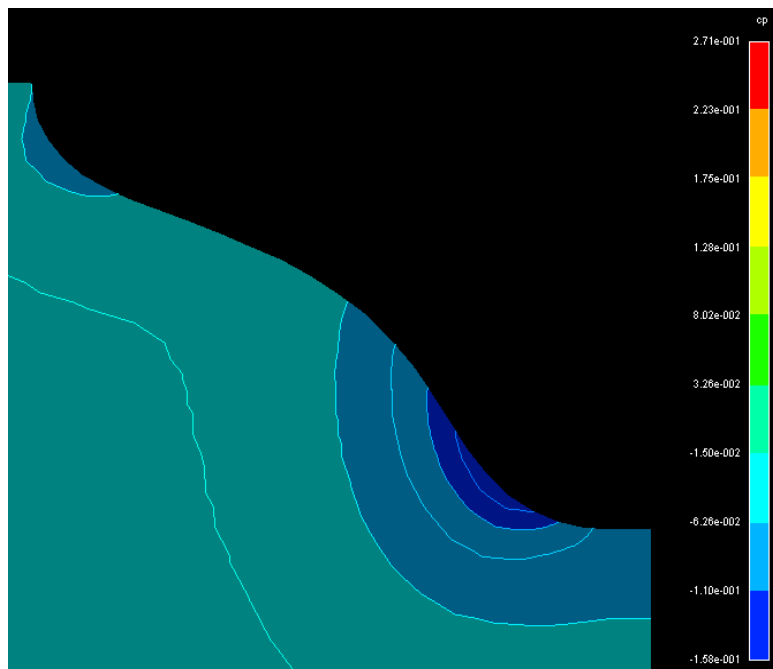


New KCS ( Developed Hull Form)

Fig. 21 Comparison of Wave profile and Wave pattern at 26knots

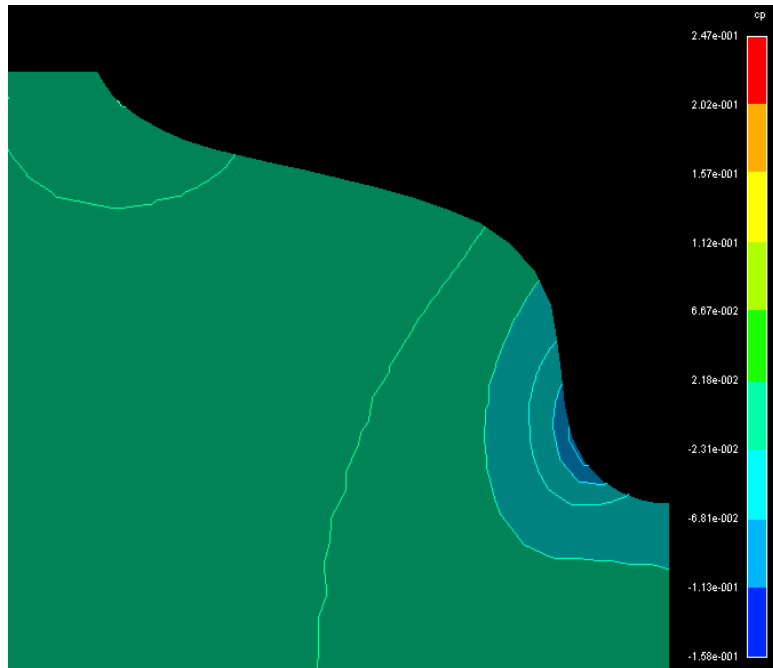


KCS (Original Hull form)

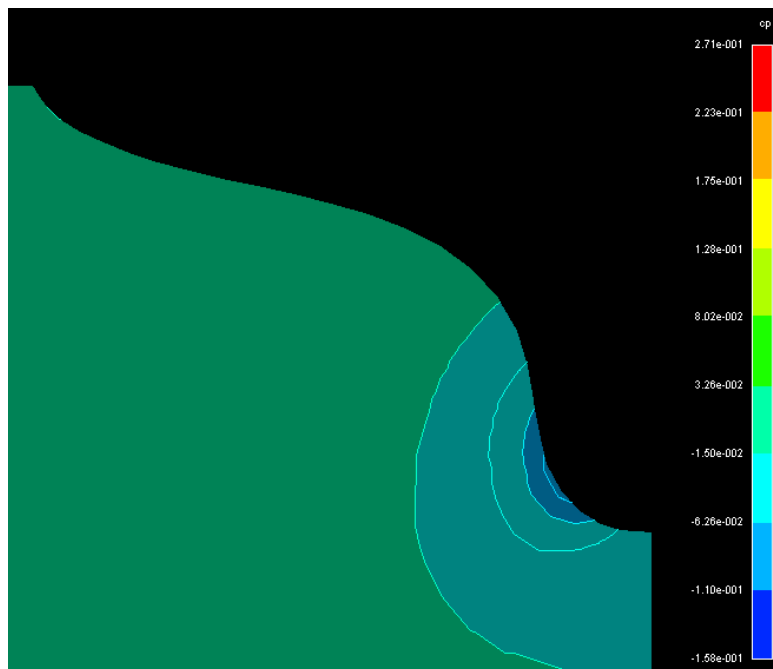


New KCS ( Developed Hull Form)

Fig. 22 Comparison of Dynamic Pressure Coefficient at Station 3 ( $x=0.85$ )



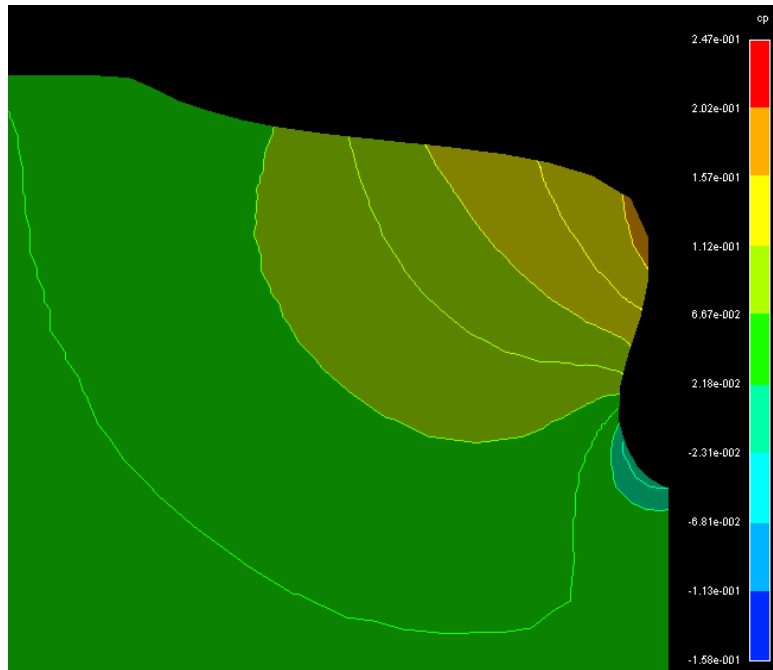
KCS (Original Hull form)



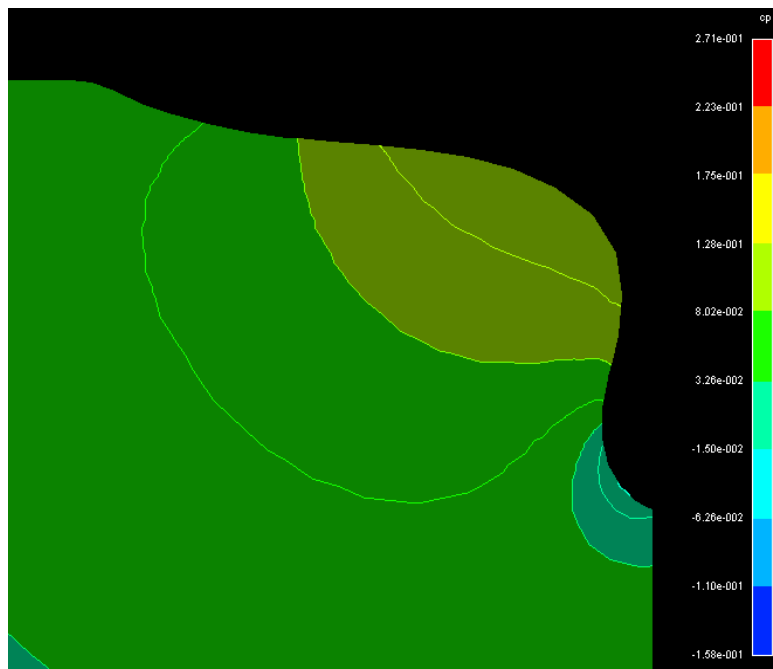
New KCS ( Developed Hull Form)

Fig. 23 Comparison of Dynamic Pressure Coefficient at Station 2 ( $x=0.9$ )



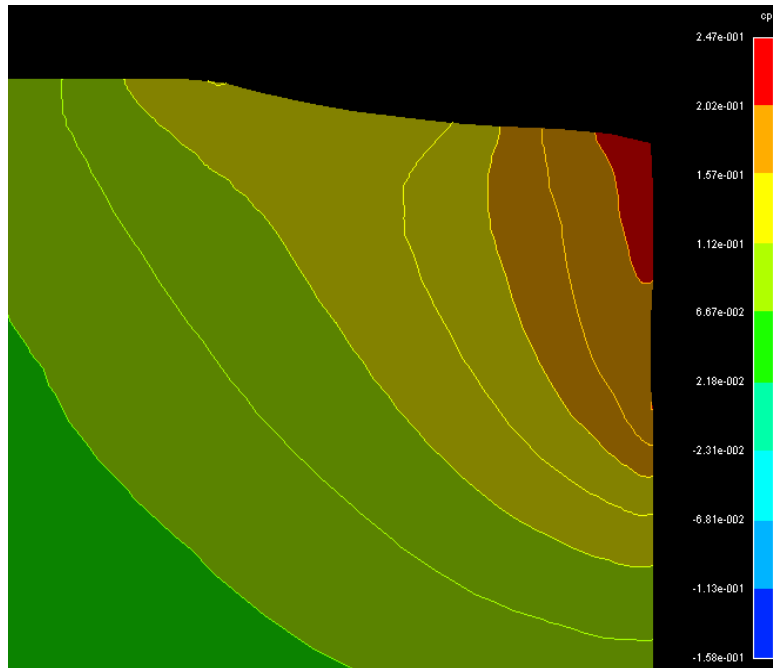


KCS (Original Hull form)

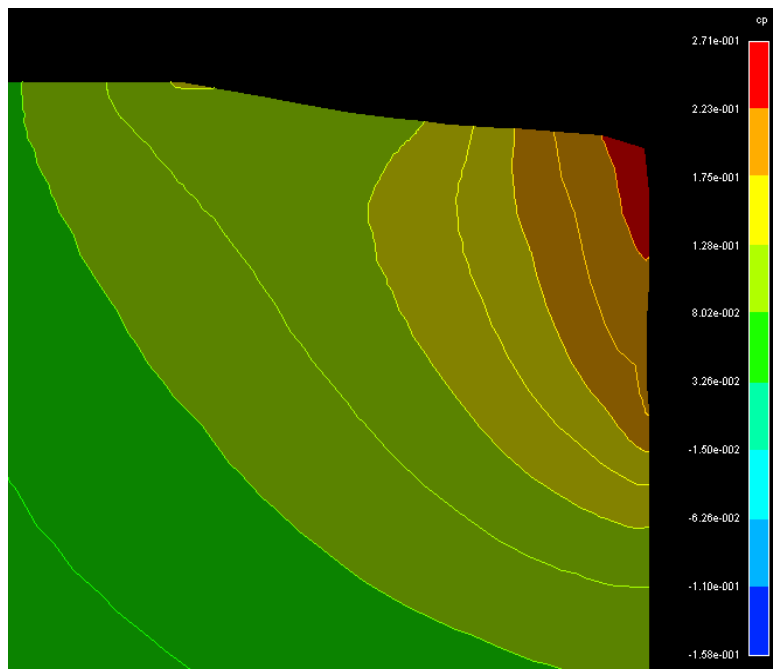


New KCS ( Developed Hull Form)

Fig. 24 Comparison of Dynamic Pressure Coefficient at Station 1 ( $x=0.95$ )

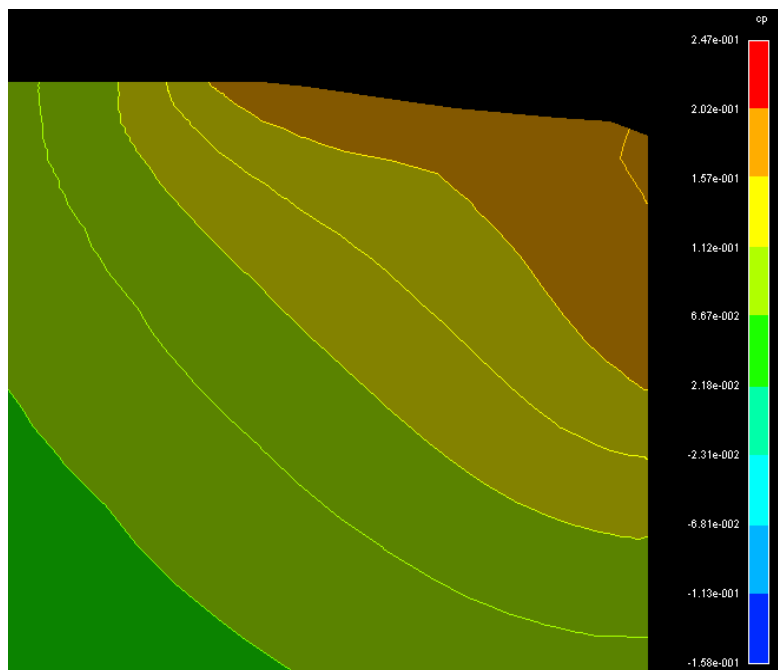


KCS (Original Hull form)

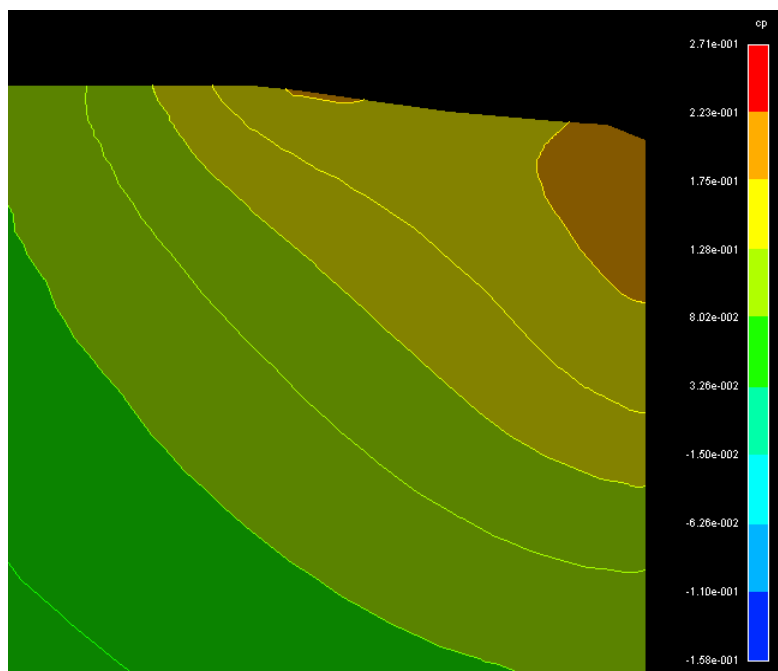


New KCS ( Developed Hull Form)

Fig. 25 Comparison of Dynamic Pressure Coefficient at propeller plane ( $x=0.98625$ )

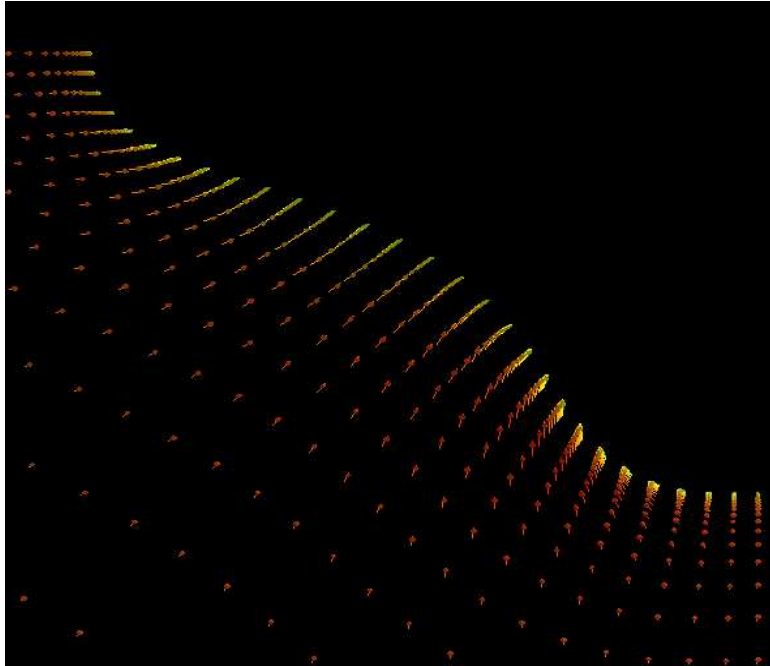


KCS (Original Hull form)

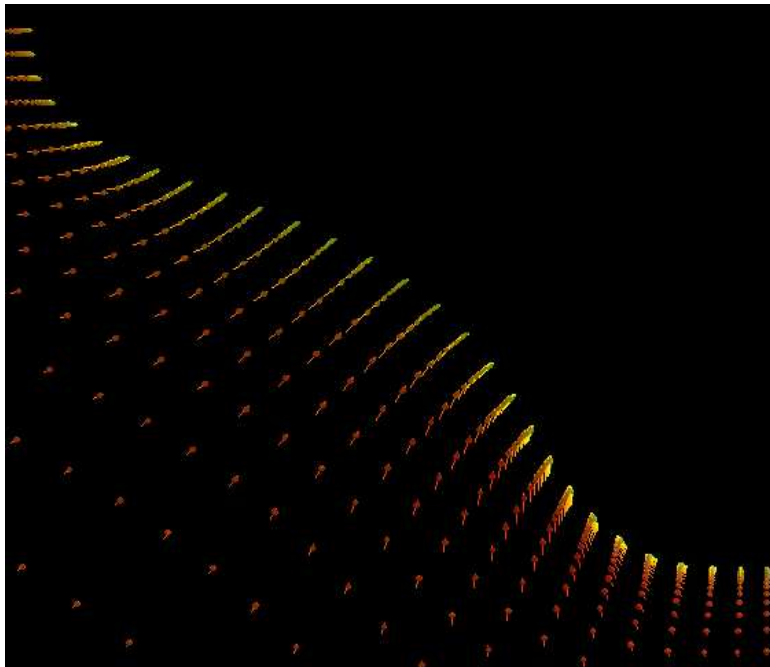


New KCS ( Developed Hull Form)

Fig. 26 Comparison of Dynamic Pressure Coefficient at AP (x=1.0)

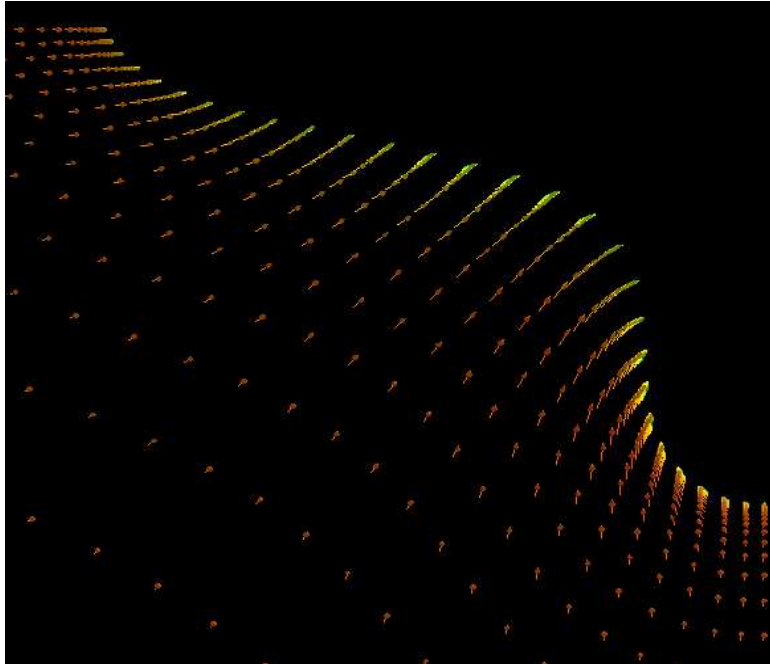


KCS (Original Hull form)

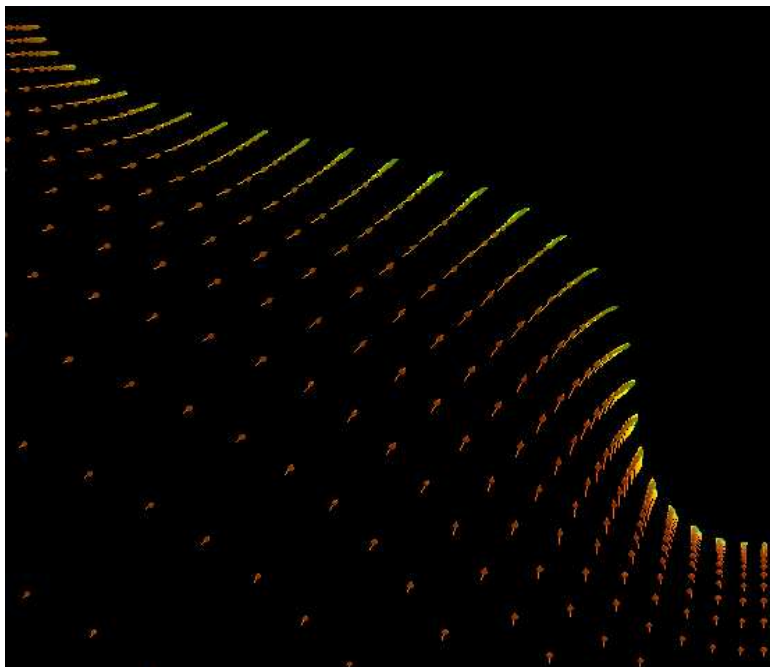


New KCS ( Developed Hull Form)

Fig. 27 Comparison of Velocity vectors at Station 3 ( $x=0.85$ )

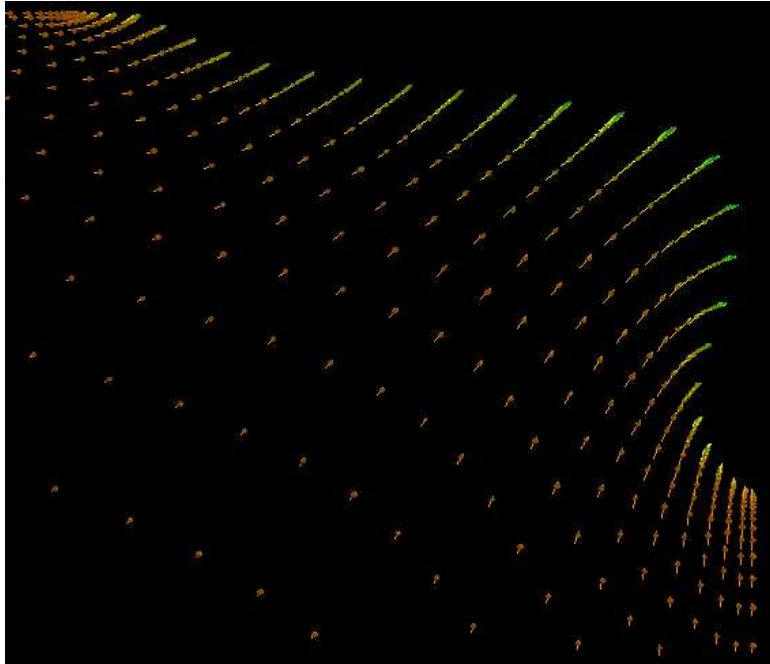


KCS (Original Hull form)

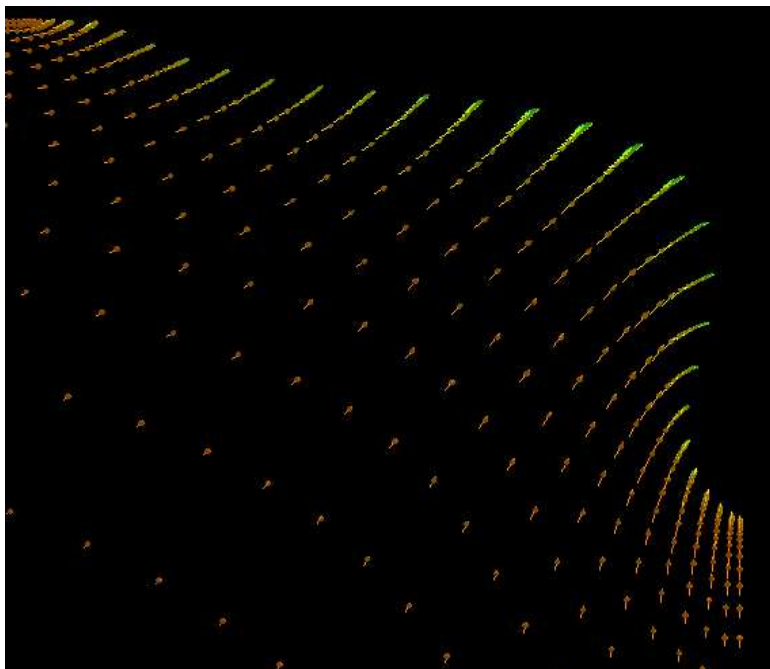


New KCS ( Developed Hull Form)

Fig. 28 Comparison of Velocity vectors at station 2 ( $x=0.9$ )

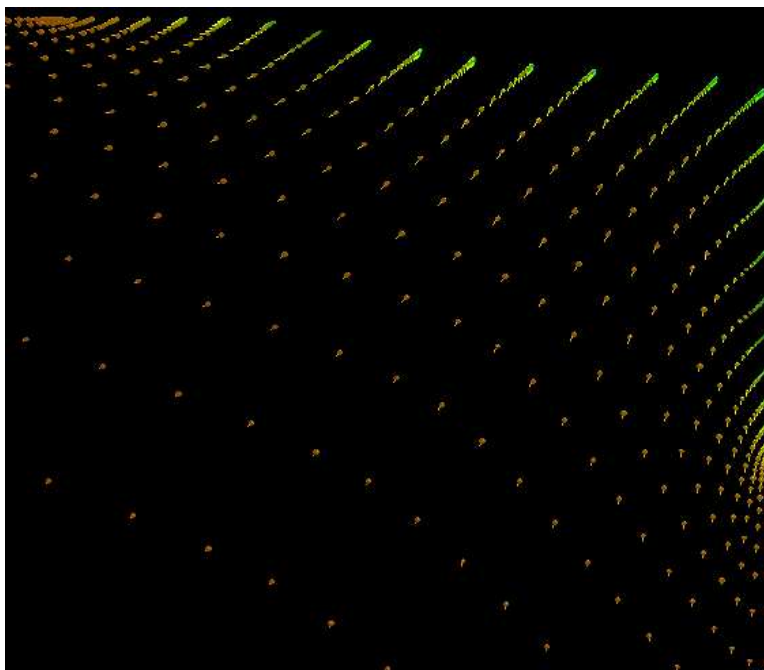


KCS (Original Hull form)

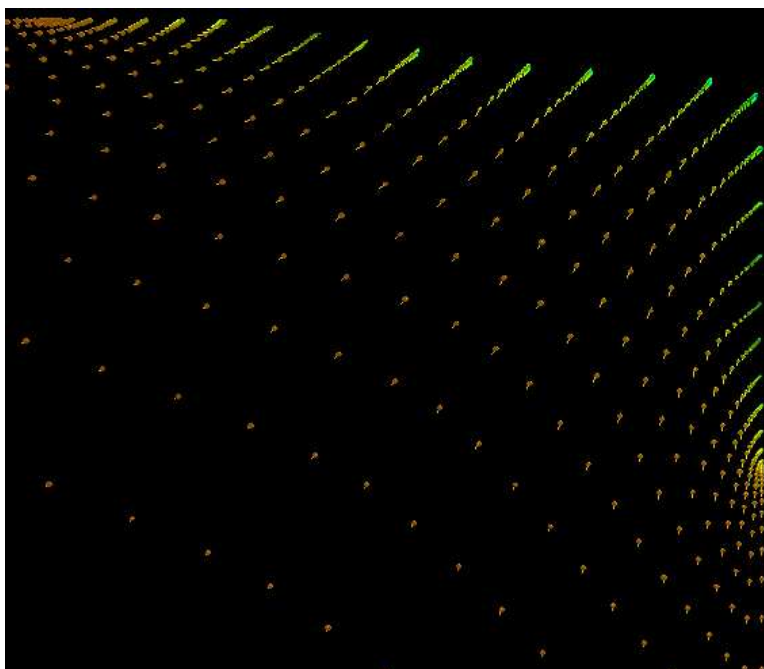


New KCS ( Developed Hull Form)

Fig. 29 Comparison of Velocity vectors at Station 1 ( $x=0.95$ )

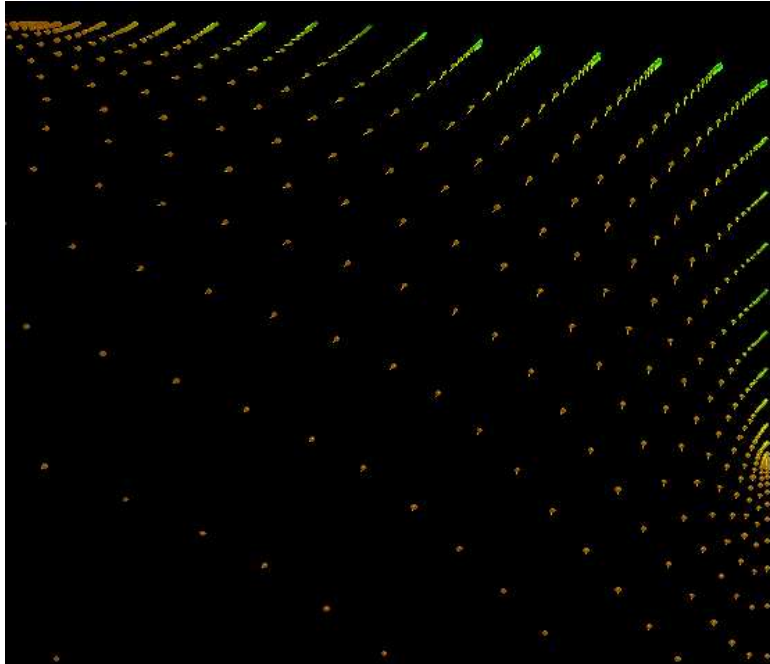


KCS (Original Hull form)

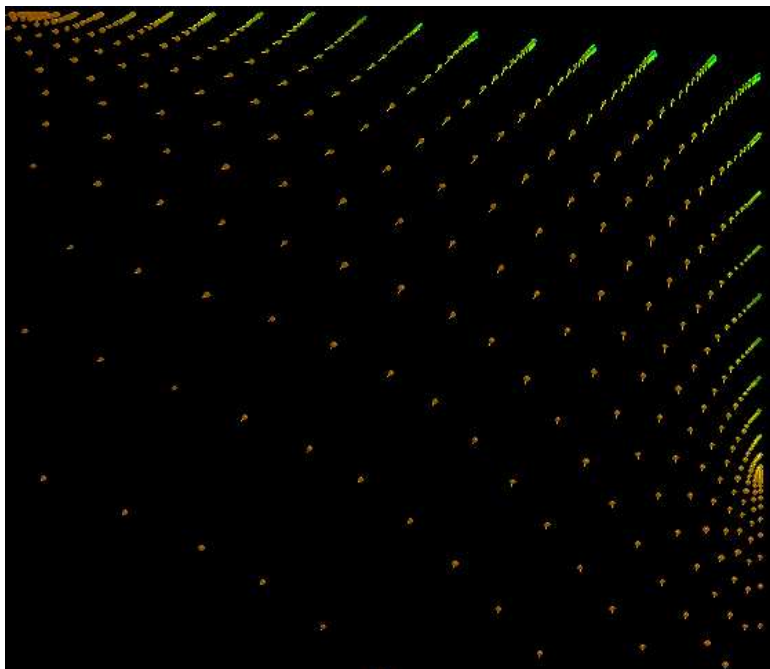


New KCS ( Developed Hull Form)

Fig. 30 Comparison of Velocity vectors at propeller plane ( $x=0.98625$ )



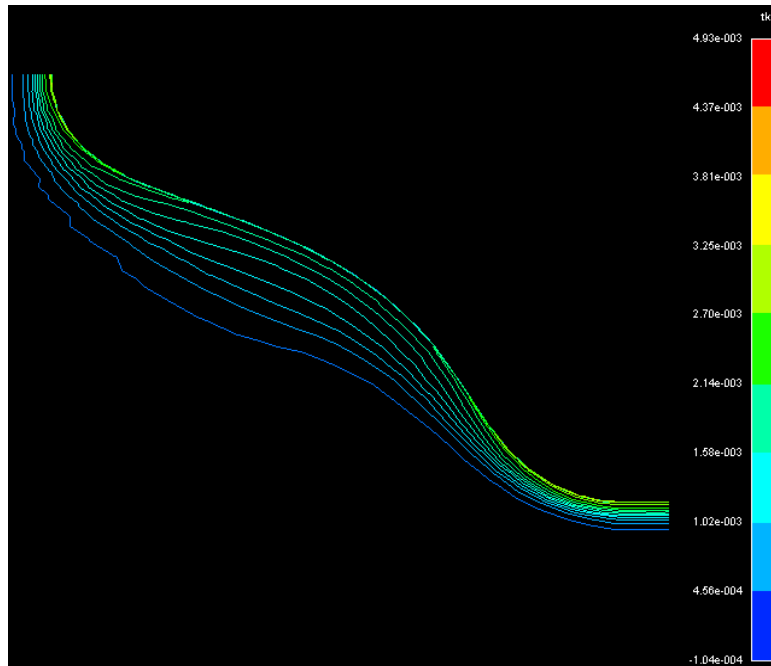
KCS (Original Hull form)



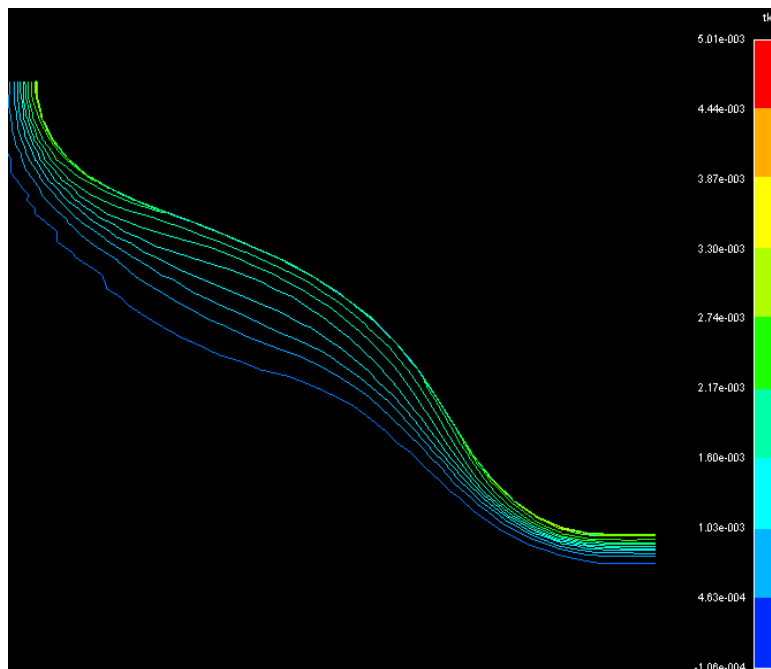
New KCS ( Developed Hull Form)

Fig. 31 Comparison of Velocity vectors at AP ( $x=1.0$ )



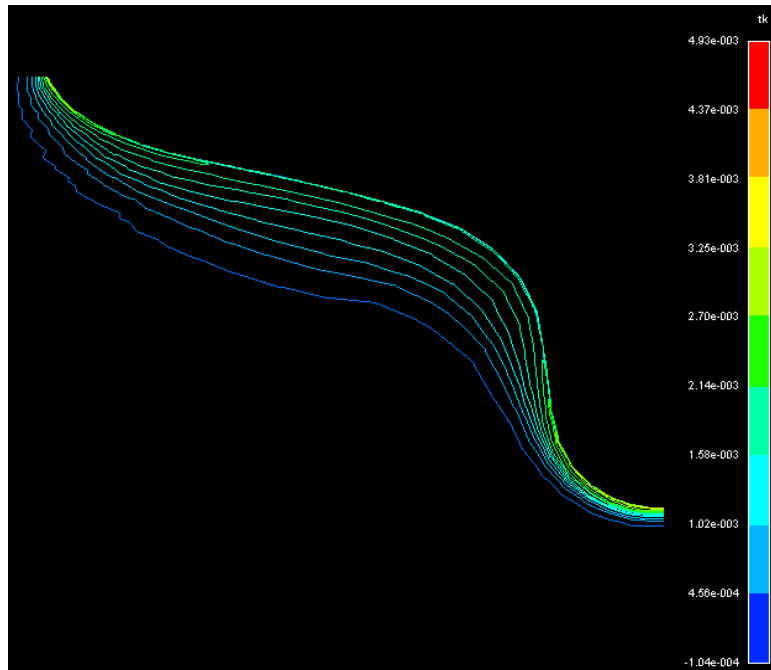


KCS (Original Hull form)

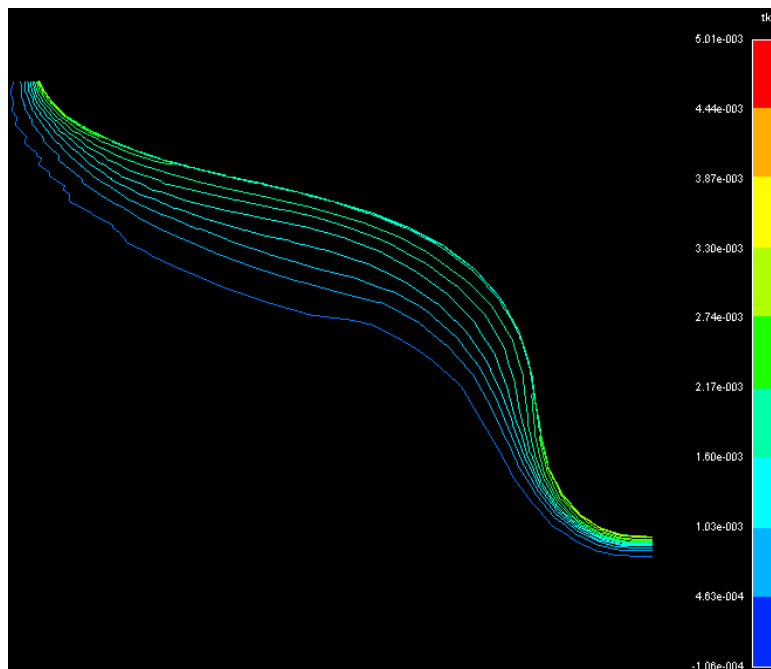


New KCS ( Developed Hull Form)

Fig. 32 Comparison of Turbulence kinetic energy at Station 3 ( $x=0.85$ )

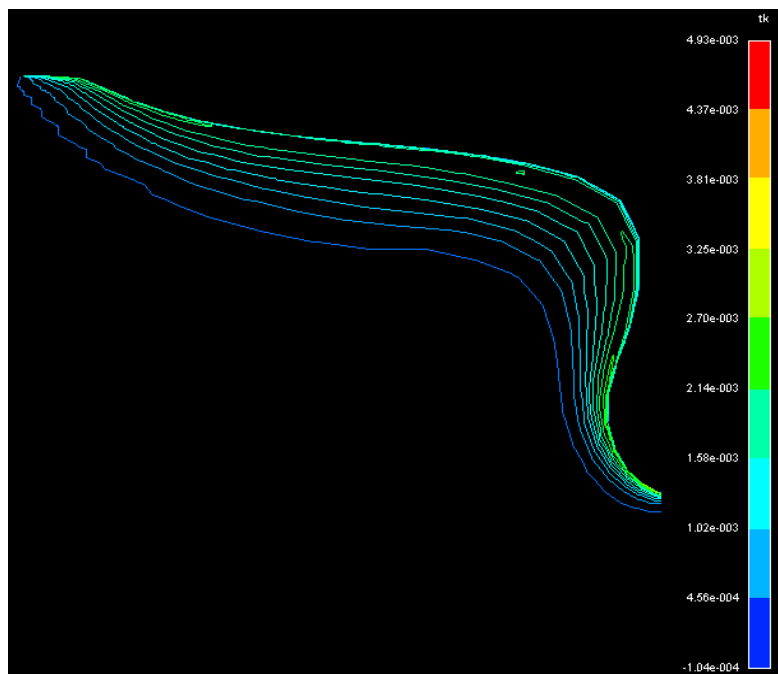


KCS (Original Hull form)

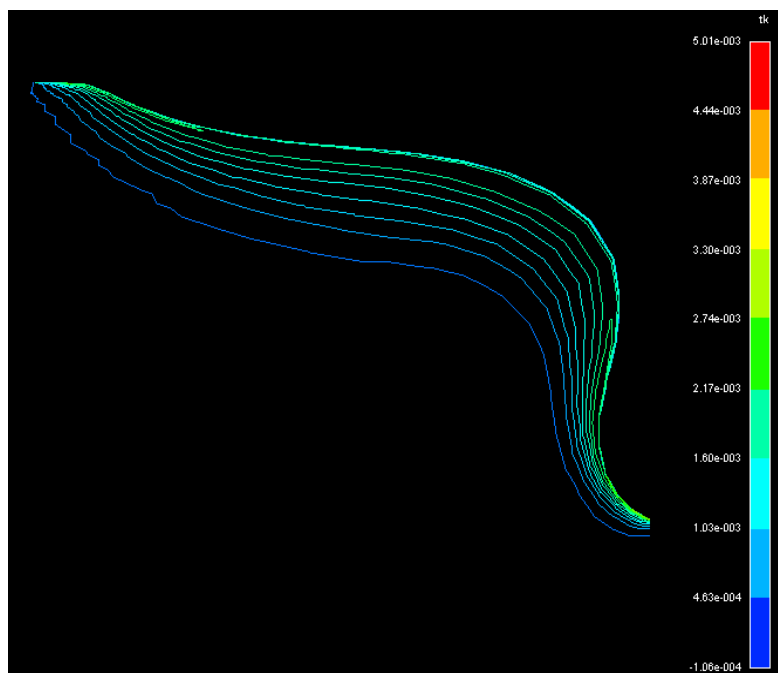


New KCS ( Developed Hull Form)

Fig. 33 Comparison of Turbulence kinetic energy at Station 2 (x=0.9)

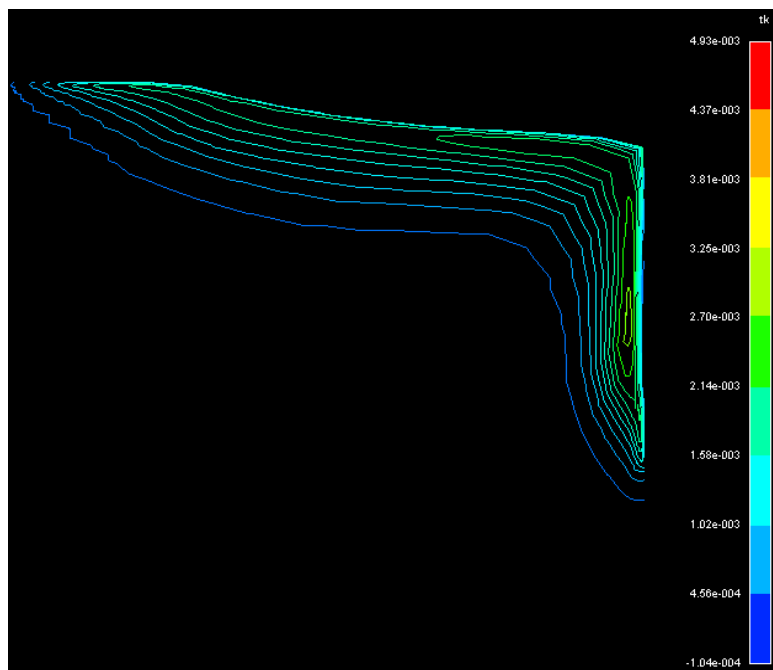


KCS (Original Hull form)

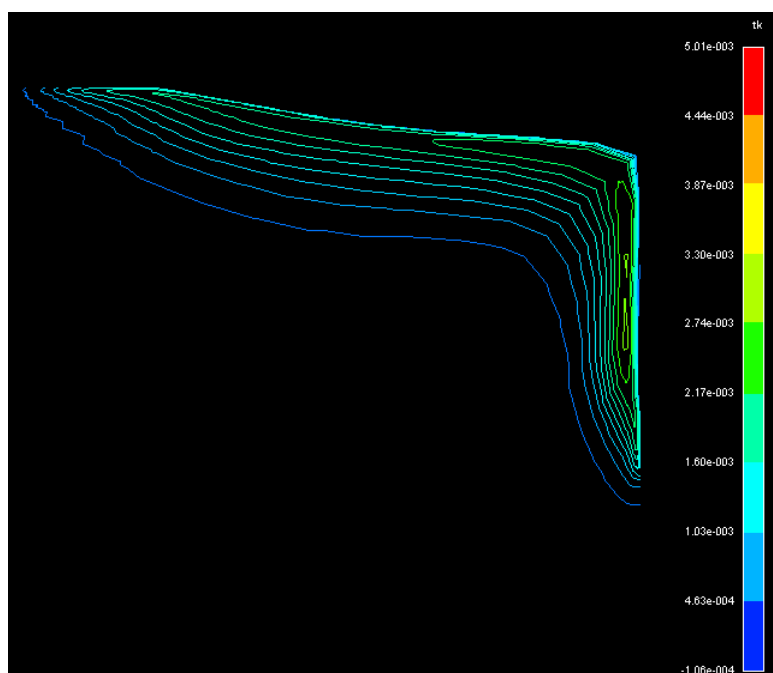


New KCS ( Developed Hull Form)

Fig. 34 Comparison of Turbulence kinetic energy at Station 1 (x=0.95)

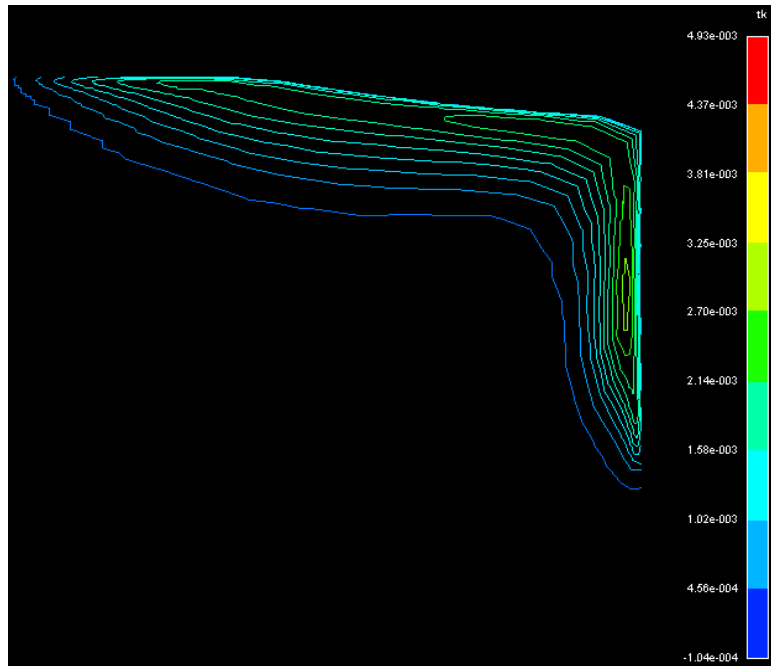


KCS (Original Hull form)

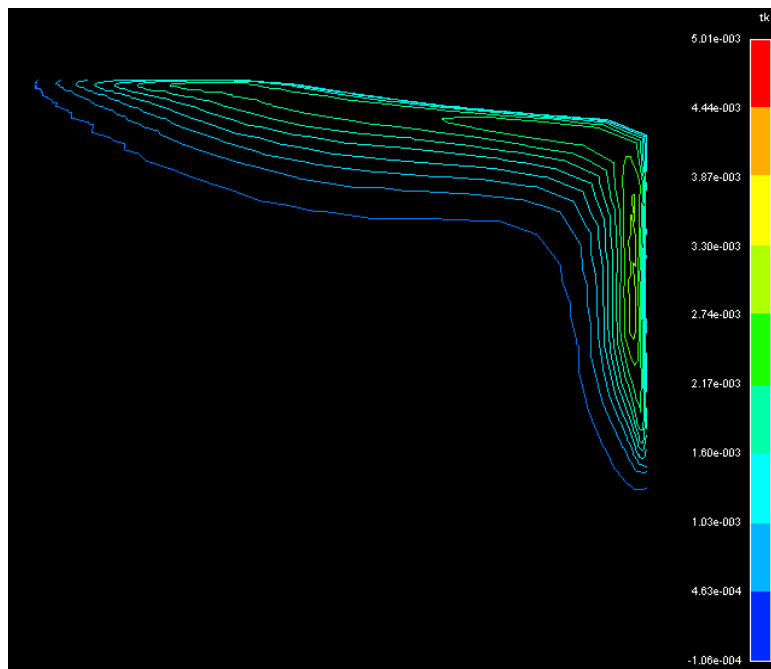


New KCS ( Developed Hull Form)

Fig. 35 Comparison of Turbulence kinetic energy at propeller plane ( $x=0.98625$ )



KCS (Original Hull form)



New KCS ( Developed Hull Form)

Fig. 36 Comparison of Turbulence kinetic energy at AP (x=1.0)

# 저작물 이용 허락서

학 과	선박해양공학과	학 번	20067120	과 정	석사
성 명	한글 조 경 훈      한문 趙 景 勳      영문 Cho Kyeong Hoon				
주 소	광주광역시 남구 봉선2동 무등APT 304동 1007호				
연락처	E-mail : karicho@nate.com				
논문제목	실험 자료의 역계산법을 이용한 선형개발				
	Hull Form Developoment by Inverse Design method of Test result				
<p>본인이 저작한 위의 저작물에 대하여 다음과 같은 조건 아래 조선대학교가 저작물을 이용할 수 있도록 허락하고 동의합니다.</p> <p style="text-align: center;">- 다                      음 -</p> <ol style="list-style-type: none"> <li>1. 저작물의 DB구축 및 인터넷을 포함한 정보통신망에의 공개를 위한 저작물의 복제, 기억장치에의 저장, 전송 등을 허락함.</li> <li>2. 위의 목적을 위하여 필요한 범위 내에서의 편집과 형식상의 변경을 허락함. 다만, 저작물의 내용변경은 금지함.</li> <li>3. 배포·전송된 저작물의 영리적 목적을 위한 복제, 저장, 전송 등은 금지함.</li> <li>4. 저작물에 대한 이용기간은 5년으로 하고, 기간종료 3개월 이내에 별도의 의사 표시가 없을 경우에는 저작물의 이용기간을 계속 연장함.</li> <li>5. 해당 저작물의 저작권을 타인에게 양도하거나 출판을 허락을 하였을 경우에는 1개월 이내에 대학에 이를 통보함.</li> <li>6. 조선대학교는 저작물 이용의 허락 이후 해당 저작물로 인하여 발생하는 타인에 의한 권리 침해에 대하여 일체의 법적 책임을 지지 않음.</li> <li>7. 소속 대학의 협정기관에 저작물의 제공 및 인터넷 등 정보통신망을 이용한 저작물의 전송·출력을 허락함.</li> </ol> <p style="text-align: center;"><b>동의여부 : 동의( ○ )      반대(      )</b></p> <p style="text-align: center;">2008년      2월      25일</p> <p style="text-align: right;">저작자: 조 경 훈      (인)</p> <p style="text-align: center;"><b>조선대학교 총장 귀하</b></p>					